Supplementary information for

Stabilizing highly-active Ru sites by suppressing lattice oxygen participation in acidic water oxidation

Yunzhou Wen[1]†, Peining Chen[1,2]†, Lu Wang[3,4]†, Shangyu Li[1]†, Ziyun Wang[2], Jehad Abed[2,5], Xinnan Mao[3], Yimeng Min[2], Cao Thang Dinh[6], Phil De Luna[2], Rui Huang[1], Longsheng Zhang[1], Lie Wang[1], Liping Wang[1], Robert J. Nielsen[4], Huihui Li[2], Taotao Zhuang[2], Changchun Ke[7], Oleksandr Voznyy[2], Yongfeng Hu[8], Youyong Li[3], William A. Goddard III[4], Bo Zhang[1]*, Huisheng Peng[1]*, and Edward H. Sargent[2]*

[1]State Key Laboratory of Molecular Engineering of Polymers, Department of Macromolecular Science and Laboratory of Advanced Materials, Fudan University, Shanghai 200438, China.

[2]Department of Electrical and Computer Engineering, University of Toronto, 10 King's College Road, Toronto, Ontario, M5S 3G4, Canada.

[3]Institute of Functional Nano & Soft Materials (FUNSOM) and Jiangsu Key Laboratory for Carbon-Based Functional Materials & Devices, Soochow University, Suzhou, 215123, China.

[4]Materials and Process Simulation Center (MSC) and Joint Center for Artificial Photosynthesis (JCAP), California Institute of Technology, Pasadena, California 91125, United States.

[5]Department of Materials Science & Engineering, University of Toronto, 27 King's College Circle, Toronto, Ontario, M5S 1A1, Canada.

[6]Department of Chemical Engineering, Queen's University, Kingston, Ontario K7L 3N6, Canada.

[7]Institute of Fuel Cell, Shanghai Jiao Tong University, 800 Dongchuan Rd., Shanghai 200240, China.

[8]Canadian Light Source Inc., Saskatoon, SK S7N 0X4, Saskatchewan, Canada.
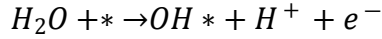
†These authors contributed equally to this work.

1   *Correspondence and requests for materials should be addressed to Edward H.
2   Sargent (ted.sargent@utoronto.ca) (E.H.S.), Huisheng Peng (penghs@fudan.edu.cn)
3   (H.S.P.) and Bo Zhang (bozhang@fudan.edu.cn) (B.Z.).
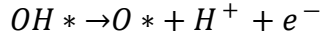4

Contents

11

12

Experimental section

Computational details. The computational high-throughput screening was performed by density functional theory (DFT) calculations. All computations were performed in the VASP package using the projector augmented wave (PAW) method to account for core−valence interactions. The PBE functional was used for the screening of structures and the PBE functional including the D3 van der Waals correction was used for the OER electrocatalytic calculations. The kinetic energy cutoff for plane wave expansions was set to 400 eV. The method of Methfessel-Paxton (MP) was applied and the width of the smearing is chosen as 0.2 eV. All the geometric structures and lattice parameters are optimized until they converge to within 3×10^{-2} eV/Å for maximal components of forces. For the optimization of the crystals, reciprocal space was sampled using the Γ-centered $3\times3\times4$ k-point mesh, while for the OER calculations on the surface structures, the K-points was used by $3\times6\times1$ mesh. The electronic density of states (DOS) was calculated using the tetrahedron method.
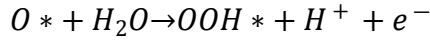
The OER reaction steps in the acidic solution and the calculated OER overpotential (η) are as following:

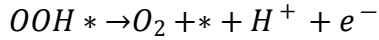$$H_2O + * \rightarrow OH* + H^+ + e^-$$
$$\Delta G_1 = G(OH*) + \frac{1}{2}G(H_2) - G(H_2O) - G(*) \tag{1}$$

$$OH* \rightarrow O* + H^+ + e^-$$
$$\Delta G_2 = G(O*) + \frac{1}{2}G(H_2) - G(OH*) \tag{2}$$

$$O* + H_2O \rightarrow OOH* + H^+ + e^-$$
$$\Delta G_3 = G(OOH*) + \frac{1}{2}G(H_2) - G(O*) - G(H_2O) \tag{3}$$

$$OOH* \rightarrow O_2 + * + H^+ + e^-$$
$$\Delta G_4 = 4.92 - \Delta G_1 - \Delta G_2 - \Delta G_3 \tag{4}$$

$$\eta = \frac{\max\{\Delta G_1, \Delta G_2, \Delta G_3, \Delta G_4\}}{e} - 1.23V \tag{5}$$

The OOH^*, O^*, and OH^* are the OER intermediates adsorbed on the catalyst surface. For each step of OER, the Gibbs free energy (ΔG) is given by $\Delta G = \Delta E_{DFT} + \Delta ZPE - T\Delta S$, where ΔE_{DFT}, ΔZPE, and ΔS are the changes in DFT total energy, zero-point energy, and entropy, respectively. The values of ΔZPE and ΔS for the gaseous phase of H_2 and H_2O are obtained from the NIST-JANAF thermodynamics table.

The $2\times2\times2$ supercell of rutile structure is adopted in our calculations for RuO_2 and ternary SrRuIr oxide compounds. We have considered ten different ratios for the ternary SrRuIr oxide compounds. 2,201 geometric configurations were optimized to search for the most stable SrRuIr oxide structures with various Sr-Ru-Ir ratios. Based on the stable crystal structures, we cleaved the (110) surface for further evaluating the OER activity. As proposed by Nørskov *et al*., we have calculated the free energies for the OER intermediates (OH, O and OOH) adsorbed on the SrRuIr oxide surface to obtain the OER overpotential.

To identify the stability of the ternary SrRuIr oxide compounds in an aqueous environment, we have calculated the Pourbaix diagrams. In a Pourbaix diagram, stable phases are mapped as a function of pH and electrochemical potential. We combined the calculated DFT energies (for the solid states) with experimentally measured dissolution energies (for the dissolved phases) to generate the Pourbaix diagram by using the ASE module. The concentration of soluble species used in the Pourbaix diagram is 10^{-6} mol L^{-1}. The thermodynamic data of involved ions was obtained from the ASE database and listed in Supplementary Table 3.

Materials. Strontium chloride hexahydrate ($SrCl_2\cdot6H_2O$), ruthenium chloride hydrate, ($RuCl_3\cdot xH_2O$) and sodium hexachloroiridate hydrate ($Na_3IrCl_6\cdot xH_2O$), Nafion® (5 wt% in a mixture of lower aliphatic alcohols and water), iridium (IV) chloride hydrate ($IrCl_4\cdot xH_2O$) and ruthenium oxide (RuO_2) and were purchased from Sigma-Aldrich or Adamas-beta. Iridium oxide (IrO_2) was provided by PERIC *Inc.* and 40% Pt/C was purchased from Johnson Matthey. N, N-dimethylformamide (DMF), ethanol, isopropanol, and acetone were purchased from Sinopharm Chemical Reagent Co., Ltd. The $H_2^{18}O$ (99%) was purchase from Nukem Isotopes. Carbon black (20 nm) were purchased from Suzhou Tanfeng Co., Ltd. The TGP-H-060 carbon paper (CP) was purchased from Toray. Freudenberg H23C9 gas diffusion layers were purchased from Fuel Cell Store. All chemicals were used without any further purification.

Synthesis of catalysts. A series of Sr-Ru-Ir ternary catalysts were synthesized by modifying previously reported sol-gel methods[1]. A typical synthesis procedure is as follows: metal salt precursors (0.3 mmol $SrCl_2\cdot6H_2O$, 0.5 mmol $RuCl_3\cdot xH_2O$, and 0.1 mmol $Na_3IrCl_6\cdot xH_2O$) were first dissolved in 2 mL DMF to form solution A. 2 mL DMF and 0.18g H_2O were mixed to form solution B. Both solution A and solution B were sealed and chilled in a refrigerator for 2h. Then, a clean stirring bar was put into solution A. 1 mL solution B and 0.5 mL propylene oxide were simultaneously dripped into solution A under stirring. The mixed solution was then sealed and aged for 1 day and black precipitates would appear. After that, the solution and precipitates were transferred into a vial and were immersed in acetone for 3 days, followed by centrifugation and washing by acetone for 6 times to thoroughly remove DMF and

propylene oxide. The as-prepared powder was dried in vacuum and then ground carefully. Afterward, the black powder was placed into a tube furnace and annealed at 500°C in the air for 1h to obtain the SrRuIr oxide catalysts. The synthesis of catalysts with different Sr:Ru:Ir ratios used the same procedure with SrRuIr. The total amount of metal salt precursors was kept as 0.9 mmol and the ratio of different precursors was varied. For the RuIr (feed ratio 5:1) and SrRu (feed ratio 3:5) samples, the same synthesis procedure was used.

Characterizations of catalysts. The high-resolution transmission electron microscopy (HR-TEM) images and corresponding energy-dispersive X-ray spectroscopy (EDX) elemental mapping were obtained from a JEOL-2100F TEM equipped with an Oxford energy disperse spectrometer. The high-angle annular dark-field scanning transmission electron microscopy (HAADF-STEM) images and corresponding EDX mappings were captured on a JEOL JEM-ARM200F aberration-corrected TEM. The X-ray photoelectron spectroscopy (XPS) measurements were conducted on a PHI 5300 X-ray photoelectron spectrometer, with a monochromatic Mg Kα X-ray sources (1253.6 eV). The XPS data was further analyzed using CasaXPS software. The binding energy was calibrated by C 1s (284.6 eV).

Electrochemical measurements. Electrochemical measurements were performed in a three-electrode system by a potentiostat (Metrohm Autolab M204), using saturated Hg/Hg_2SO_4 electrode (E^{θ} = 0.652V *vs.* RHE at 25°C) as the reference electrode and platinum foil as the counter electrode. To prepare the catalyst film on glassy carbon electrodes (GCE, 3 mm in diameter), 5 mg catalyst and 2 mg carbon black were dispersed in 1 mL mixture of water and ethanol (4:1, *v/v*), and then 40 µL of 5 wt. % Nafion® solution was added. The suspension was immersed in an ultrasonic bath for at least 60 min to obtain a homogeneous ink. After that, 4.5 µL of the catalyst ink was carefully deposited onto the GCE (catalyst loading 0.32 mg cm^{-2}). For electrochemical measurements on CPs, the catalysts were sprayed onto CPs using an airbrush. 15 mg catalysts and 3 mg carbon black were first dispersed in 2 mL isopropanol, and then 30 µL of 5 wt. % Nafion® solution was added. After at least 60 min sonication, the homogeneous ink was sprayed onto 2 cm × 2 cm CP heated to 70°C. The CPs were weighed before and after airbrush and the total catalyst loading were controlled at *ca.* 1.5 mg cm^{-2}.

To assess the OER catalytic activity, the working electrode was first scanned from 0.2 to 0.9 V *vs.* Hg/Hg_2SO_4 at a rate of 50 mV s^{-1} for 10 cycles to achieve stable cyclic voltammetry (CV) scans in 0.5 M H_2SO_4 (pH = 0.3). Then linear sweep voltammetry (LSV) with a rate of 10 mV s^{-1} was measured. All measurements were conducted at room temperature. All potentials were referred to the reversible hydrogen electrode (RHE) by the following calculations:

$$E_{RHE} = E_{Hg/Hg_2SO_4} + 0.652 + 0.0591 \times pH = E_{Hg/Hg_2SO_4} + 0.6697$$

All the potentials were applied a 95% iR compensation. The uncompensated solution resistances were measured by electrochemical impedance spectra (EIS), which were conducted at a bias of 1.40V *vs*. RHE in the frequency range from 100 kHz to 10 mHz with an amplitude of 5 mV.

The steady-state Tafel plots were measured by chronoamperometry on rotation disk electrodes (1,600 rpm). The sample was held at constant potential from 1.25 V to 1.75V *vs*. RHE with a step of 20 mV. Each potential step was retained for 10 s to reach stable and the final current was recorded.

ECSA was deduced from electrochemical double-layer capacitance (C_{dl}) by dividing a factor of 0.035 mF cm^{-2}, according to the previous report[2]. The measurement of C_{dl} was carried out by cyclic voltammetry (CV) at the non-Faradic region. The catalysts were scanned at a range of +0.25 to +0.35 V *vs*. Hg/Hg$_2$SO$_4$ using elevated scan rates. Both anodic and cathodic current at 0.3 V *vs*. Hg/Hg$_2$SO$_4$ were plotted against scan rates (**Error! Reference source not found.** and **Error! Reference source not found.**). Then, linear fitting was adopted to these points, and the average slope of anodic and cathodic plots represented the value of C_{dl}.

To eliminate the interference of bubble accumulation and mechanical peeling of catalysts, the OER stability was evaluated on carbon paper by chronopotentiometry at 10 mA cm$^{-2}_{geo}$. The electrochemical cell was placed in a 25°C thermostatic water bath. The electrolyte was replaced every four days to keep the pH of the electrolyte stable. All v-t plots were 95% iR-compensated. To verify the stability of our test platform in harsh acidic conditions, we first carried out the chronopotentiometry on IrO$_2$. The overpotential of IrO$_2$ was quite stable. We manually stopped the test after 70h. This result confirms that the decay of activity mainly comes from the catalysts in our experiments. In the calculation of the degradation rate, we regarded the first 10% of the total test time as burning time, ensuring the catalysts reaching stable.

The stability number (S-number) was calculated according to ref.[3], using the following equation:

$$S\_number = \frac{n_{O_2}}{n_{noble\ metal}}$$

Where n_{O_2} is the molar number of total oxygen evolved within a certain period of time (calculated from total charge), $n_{noble\ metal}$ is the total noble metal dissolved measured by ICP-OES.

ICP-OES analysis of the ion dissolution. The dissolution of catalysts during OER process was quantified by inductively coupled plasma optical emission spectrometry (ICP-OES, iCAP7400, Thermo Fisher). The catalyst was air-brushed onto carbon paper with a catalyst loading of *ca.* 1.5 mg cm^{-2} and electrolysis at 10 mA cm^{-2} (Specifically, the sample demonstrated in Figure 2f was 1 cm^2 in area). A low volume (10 mL) of

1   electrolyte was used to fulfill the limit of detection of the equipment. The electrolyte

2   was sampled after 0.5h, 2h, 6h, 12h and 24h electrolysis. At each sampling point, 4 mL

3   of electrolyte was taken out for ICP measurement and refilled to 10 mL with clean

4   electrolyte before the next sampling period.

5

6   **X-ray absorption spectroscopy.** *Ex-situ* Ru K-edge and Ir L_3-edge XANES and

7   EXAFS of post-OER catalysts were performed in fluorescent mode at BL14W1

8   beamline of Shanghai Synchrotron Radiation Facility (SSRF), using a Si(311)

9   monochromator. The *in situ* Ru K-edge and Ir L_3-edge measurements were carried out

10   at 1W1B beamline in Beijing Synchrotron Radiation Facility (BSRF). A home-made

11   triangular electrochemical cell was used, which was equipped with a three-electrode

12   configuration. The electrochemical cell was placed in the middle of the optical path

13   with an incident angle of 45°. The working electrodes were prepared by spray coating

14   the catalysts on carbon paper. During the *in-situ* measurements, chronoamperometry

15   processes at 1.35 V *vs*. RHE were employed and the fluorescent mode was used to

16   acquire data. The energy of Ru K-edge was calibrated by Ru foil and the energy of Ir

17   L_3-edge was calibrated by Pt foil. The *in-situ* Ru L_3-edge XAS spectra were acquired

18   at SXRMB beamline in Canadian Light Source (CLS), Canada. To perform the *in-situ*

19   soft X-ray measurements, the electrochemical cell was carefully sealed and placed in

20   the helium atmosphere to reduce X-rays attenuation. All XAS data were processed and

21   normalized by ATHENA software included in IFEFFIT software package[4]. As to the

22   fitting and simulation of EXAFS data, the ARTEMIS software and FEFF8.5 codes were

23   used. The detailed discussion of EXAFS fitting is presented in Supplementary note 2.

24

25   **Differential electrochemical mass spectroscopy (DEMS) measurements.** DEMS

26   measurements were carried out to determine the ^{18}O-labeled volatile reaction products

27   of SrRuIr and RuO_2 catalysts during OER process using a QAS 100 device (Linglu

28   Instruments, Shanghai). A saturated Ag/AgCl electrode and a Pt wire were used as

29   reference electrode and counter electrode, respectively. The working electrodes were

30   prepared by sputtering Au onto 50 μm thick porus PTFE films. Then, the catalysts

31   were drop cast onto the Au with a loading mass of 0.65 mg cm^{-2}. First, the catalysts

32   were labeled with ^{18}O isotopes by performing 5 CV cycles at a scan rate of 5 mV/s in

33   ^{18}O-labed 0.5M H_2SO_4 (Since the activity of SrRuIr was much higher than RuO_2, so

34   the potential window was 1 V-1.35 V *vs*. Ag/AgCl for SrRuIr and 1V -1.6 V *vs*.

35   Ag/AgCl for RuO_2. So that both catalysts can reach a similar current for direct

36   comparison.). Afterwards, ^{18}O-labeled electrodes were rinsed with ^{16}O water for five

37   times to remove the remaining $H_2^{18}O$. Finally, the electrodes were carried out CV cycles

38   in ^{16}O H_2SO_4 solution at the above potential window and scan rate. At the mean time,

39   gas products of different molecular weights generated during OER process were

40   measured in real time by mass spectroscopy. Since catalysts were thoroughly rinsed

with ^{16}O water after ^{18}O-labelling, it is unlikely that ^{18}O species adsorbed on the surface contribute substantially to the observed $^{34}O_2$ ($^{16}O^{18}O$) signals. Thus, it can be determined to investigate the participation of lattice oxygen from catalysts in OER by measuring the $^{34}O_2$ signals.

In situ Raman spectroscopy. The in situ electrochemical Raman spectroscopy measurements were carried out to investigate the participation of lattice oxygen during OER. The spectra were acquired by a Horiba XploRA Raman spectrometer equipped with a 50× objective and 20 mW 532 nm laser. The collection was carried out at 20 s exposure time averaged over 5 exposures. A home-made PTFE electrochemical cell was used in the in situ measurements. The thickness of the electrolyte layer was controlled at ~0.6 mm. A saturated Ag/AgCl electrode and a Pt wire were used as reference electrode and counter electrode, respectively. The working electrodes were prepared by drop-casting the catalysts ink onto a 0.25 mm thick Ti foil (Alfa Aesar). The Raman spectra were collected along with the chronoamperometry measurements. The applied potential was elevated from OCP to 1.4 V vs. RHE. For each potential, at least three different points were measured. The above measurements were carried out in both ordinary 0.5 M H_2SO_4 and ^{18}O labeled H_2SO_4 solution.

PEM electrolyzer test. A catalyst-coated membrane (CCM) method was used to prepare the anode layer of the membrane electrode assembly (MEA). The anode catalyst was first dispersed in a mixture of isopropanol and Nafion® solution, and the ionomer amount was 20 wt. %. After adequate sonication, the homogeneous inks were sprayed onto a piece of 50 μm polytetrafluoroethylene (PTFE) film. The CCM was obtained by transferring the catalyst layer from the PTFE film to a Nafion® NR212 membrane using the decal method (140°C, 2.5 Mpa for 2 min). The CCM was then boiled in 0.5 M H_2SO_4 and DI water to remove impurities. For cathode, a catalyst-coated diffusion layer was used. 40% Pt/C was used as a cathodic catalyst and sprayed onto a Freudenberg H23C9 gas diffusion layer. The ionomer amount in the cathode was 30 wt. %. The mass loadings were controlled at 2 mg_{cat} cm^{-2} and 0.2 mg_{Pt} cm^{-2} for anodic and cathodic catalysts, respectively. A porous sintering Ti plate was used as porous transport layer (PTL) for anode. Finally, the cell was integrated by pressing cathodic diffusion layer, CCM, PTL and two Ti end-plate with flow field together. The active area was regarded as 2.85 cm^2, which was the area covered by the serpentine flow channel. During the test, the cell was maintained at 80°C, and the pre-heated DI water was fed to the anode at a flow rate of 40 ml min^{-1}. Before the polarization test, the cell was activated for 1h at 1 A cm^{-2}. The steady-state polarization curve was collected at galvanostatic mode from 0.1 to 2 A cm^{-1}. Each step was 0.1 A cm^{-1} and maintained for 1 min until the cell voltage was stable.

Supplementary Notes

Supplementary Note 1: Turnover frequency (TOF) calculations

In this work, the measurements of TOF for different catalysts were carried out on glassy carbon electrodes (GCE).

TOF is defined as the frequency of reaction on per active site, which is used to compare the intrinsic activity of different catalysts. TOF value in this study was calculated by the equation:

$$TOF = \frac{j \times A \times \eta}{4 \times e \times n}$$

where j is the current density at overpotential = 300 mV after 95% iR compensation and capacitance current correction, A is the geometric area of GCE (0.0706 cm^2), η is the Faradic efficiency and e is the charge of electron (1.602×10^{-19} C) and n is the number of active site.

We determined the active site number n *via* the total loading mass by assuming all nobel metall atoms as active sites (underestimating case), according to the following equation:

$$n_{mass} = \frac{m_{loading} \times N_A}{Mw} \times n_{Ru}$$

where $m_{loading}$ is the loading mass. N_A is Avogadro's constant (6.022×10^{23} mol^{-1}), Mw is the molecular weight of catalysts and n_{Ru} is the number of Ru atom per molar of catalysts.

As can be seen in Supplementary Table 5, the activity trends are SrRuIr ≥ SrRu ≥ RuIr ≥ RuO$_2$ ≥ IrO$_2$. **The above result verified the high intrinsic activity of SrRuIr.**

Supplementary Note 2: XAS measurements and analysis

For Ru K-edge data, the absorption edge energy E$_0$ of pure Ru foil was aligned to 22117 eV. E$_0$ of Ru foil was assigned by the first maximum of first-derivative X-ray absorption near-edge structures (XANES) spectrum. All data were aligned according to the standard Ru foil. For Ir L$_3$-edge data, a Pt foil was used as a standard sample. The E$_0$ of Pt L$_3$-edge was assigned to 11564 eV. All Ir L$_3$-edge data was calibrated according to the standard Pt sample. The spectra plotted in *k*-space demomstrated good signal-to-noise ratio (Supplementary Figure 44).

The wavelet transform of extended X-ray absorption fine structure (WT-EXAFS) analysis is a useful method to identify scatters from different elements with similar bond lengths, which were very suitable to the multi-metal system like SrRuIr[5-6]. In this work, the WT-EXAFS diagram was performed by *WTEXAFS* software written by Zhaoming Xia[7]. We used the Morlet wavelet to perform the transformation of EXAFS. Two parameters η and σ can be adjusted in the Morlet wavelet function to achieve the best spatial resolution. Usually, the range of parameters is 4 ≤ η ≤ 15, 0.4 ≤ σ ≤ 2, respectively[6]. We adopted η = 6.8, σ = 0.5 for Ru K-edge and η = 8.5, σ = 1 for Ir L$_3$-

1 edge during the analysis of SrRuIr. Besides, combining *ab initio* FEFF calculation with
2 WT analysis could achieve more accurate results[8]. Unfortunately, due to the similar
3 atomic number and small doping quantity, the Ru-Sr scattering could hardly be
4 identified from WT-EXAFS, as was illustrated by *ab initio* calculation of scattering
5 paths (Supplementary Figure 19).

6   The simulation of the EXAFS spectra of SrRuIr was carried out by the FEFF 8.5
7 codes embedded in the *Artemis* software. The crystallographic information file (CIF)
8 of RuO_2, was used as primary models to calculate raw scattering paths[9]. Ru-Ir, Ru-Sr,
9 and Ir-Ru scattering paths were created by replacing corresponding Ru atoms in the
10 FEFF input file (Supplementary Figure 45 and Supplementary Figure 46). The
11 experimental spectra were fitted by raw scattering paths at a k-range of 3.5 to 13.5 Å^{-1},
12 and selected path and fitting parameters are presented in Supplementary Table 9.

13   The following criteria were adopted during the fits to rationalize and simplify the
14 process:

15   (i)   The passive electron reduction factor S_0^2 was set as the same for all paths;
16   (ii)   Energy shifts of E_0 for Ru, Ir, and Sr were set as the same;
17   (iii)   One mean squared displacement σ_i^2 was used for Ru, Ir, and Sr;
18   (iv)   For the first shell fitting of Ru K-edge, two O scattering paths were used, and
19   the degeneracy (N) ratio was set as 1:2, representing two kinds of oxygen
20   atoms in the octahedron;
21   (v)   The N ratio of Ru:Ir was set as 4:1, according to atomic ratio Ru:Ir = 5:1 (the
22   scattering center was the fifth Ru atom);
23   (vi)   The degeneracy of second shell O was fixed at 4.
24   (vii)   The N value of Sr after reaction could hardly be determined, so we set
25     $N_{Sr}=0.25 \times N_{Ru}$, which was the most stable ratio according to the theoretic
26   Pourbaix diagram.
27   (viii)   The Ir-Sr scattering path was not considered in Ir L_3-edge fitting, for the
28   possibility of Ir-Sr scattering was very low at such low doping concentration.
29

30 **Supplementary Note 3: Leaching of Sr**
31   Leaching of Sr and its impact are discussed in many papers involving Sr oxides and
32 perovskites. For example, Seitz *et al.* argued that the Sr-deficient IrO_x/$SrIrO_3$ surface
33 was highly active towards OER[10], while Chang *et al.* pointed out that the chemical
34 corrosion of Sr atom was induced by the formation of unstable Ru^{n+}(n>4) in Strontium
35 Ruthenate[11].

36   In this work, we examined the status of Sr in SrRuIr both theoretically and
37 experimentally. During the DFT materials screening, we found that the doping of Ir
38 does not alter the RuO_2 lattice significantly while increasing the doping of Sr will
39 induce the structural distortion (Supplementary Figure 38). This is reasonable since the
40 similar lattice parameters of Ru oxides and Ir oxides, but Sr oxides are much different.

1   This hinted that the structural order may increase once Sr leached from the materials.
2   In the Pourbaix diagram calculations, we noticed that the most OER active $Sr_2Ru_5Ir_1O_{16}$
3   phase is not stable under OER condition, part of Sr will leach into the solution and form
4   a stable Sr-Ru-Ir ternary phase ($Sr_1Ru_6Ir_1O_{16}$ phase in our DFT prediction).

5   To verify the DFT predictions, we carefully examined the content of Sr in SrRuIr
6   catalyst after OER. According to the time-dependent ICP-OES data (Figure 2f), the
7   content of Sr in the material didn't change significantly after 12 h OER. The Sr:Ru:Ir
8   ratio was around 0.33:5:1 after 24 h OER. The XPS survey of Sr 3d demonstrated
9   similar results: The surface Sr:Ru:Ir ratio is 0.44:5:1.95 after 12-h OER and 0.38:5:1.60
10 after 24 h (Supplementary Table 12). Along with the OER process, surface Sr decreased
11 and almost disappeared after 24 hours, while most of the lattice Sr were retained after
12 24 h OER[12] (Supplementary Figure 39). The STEM-EDX mapping of SrRuIr after 24
13 h OER also demonstrated the presence of Sr in the catalysts (Supplementary Figure 17),
14 the Sr:Ru:Ir ratio was quantified as 0.36:5:1.14. All three methods showed similar
15 results on the content of Sr, which indicated that a stable Sr-Ru-Ir ternary phase may
16 form during OER process, as was predicted by DFT calculations. The composition of
17 this phase can be roughly described as $Sr_{0.35}Ru_5Ir_{1.2}O_x$ (calculated according to the
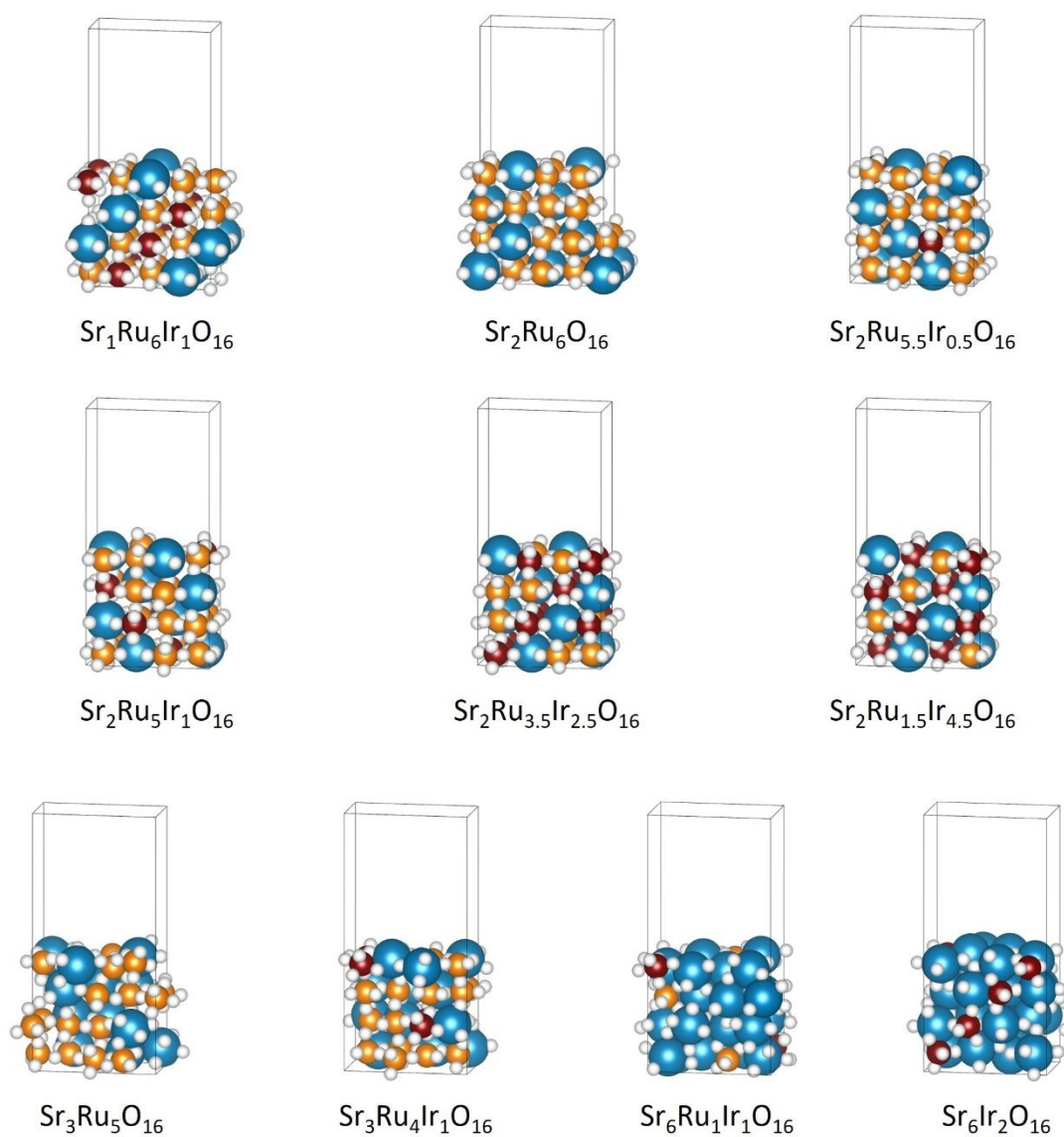18 average ratio of ICP, EDX and XPS).

19 The effect of Sr leaching towards the electronic structure of active Ru sites was
20 then examined by the theoretical PDOS calculations (Figure 4c). As Sr decreased, the
21 donation of the unoccupied e_g state into Ru d band decreased accordingly. The Bader
22 charge of the active Ru sites also decreased (Supplementary Table 13), indicating less
23 high-valence Ru sites could form, thus leading to the drop of OER activity. Additionally,
24 as indicated by the HR-TEM and EXAFS after OER (Supplementary Figure 17 and
25 Supplementary Figure 21), the leaching of Sr may lead to an increase in the size and
26 crystallinity of SrRuIr catalysts, which may also account for the activity loss.
27

28 **Supplementary Note 4: The effect of solvent in DFT calculations**
29 To investigate the effect of solvent during OER and its impact on the dissolution
30 of Sr and Ru ions, we calculated the OER pathway of RuO_2 based on explicit solvent
31 models (Supplementary Figure 36). These models include two monolayers of H_2O
32 molecules. The energetics of these models are presented in Supplementary Figure 37.
33 The theoretical overpotential does not change significantly compared to the models
34 without solvent.
35 The effect of solvent on OER is also discussed by Norskov *et al.* on the (110)
36 surface of IrO_2 using explicit solvent models[13]. They concluded that the energetics of
37 the reaction pathway are relatively unchanged with the inclusion of explicit solvent,
38 which is close to our results. The predictions of OER activity by DFT are not strongly
39 affected by solvent.
40

1 Supplementary Figures (Supplementary Figure 1-
2 Supplementary Figure 46)
3

$Sr_1Ru_6Ir_1O_{16}$ $Sr_2Ru_6O_{16}$ $Sr_2Ru_{5.5}Ir_{0.5}O_{16}$

$Sr_2Ru_5Ir_1O_{16}$ $Sr_2Ru_{3.5}Ir_{2.5}O_{16}$ $Sr_2Ru_{1.5}Ir_{4.5}O_{16}$

$Sr_3Ru_5O_{16}$ $Sr_3Ru_4Ir_1O_{16}$ $Sr_6Ru_1Ir_1O_{16}$ $Sr_6Ir_2O_{16}$

4
5 **Supplementary Figure 1 | Optimal surface structures of SrRuIr oxide with**
6 **different Sr-Ru-Ir ratios.** Blue balls – Sr, orange balls – Ru, brown balls – Ir, white
7 balls – O.
8

1
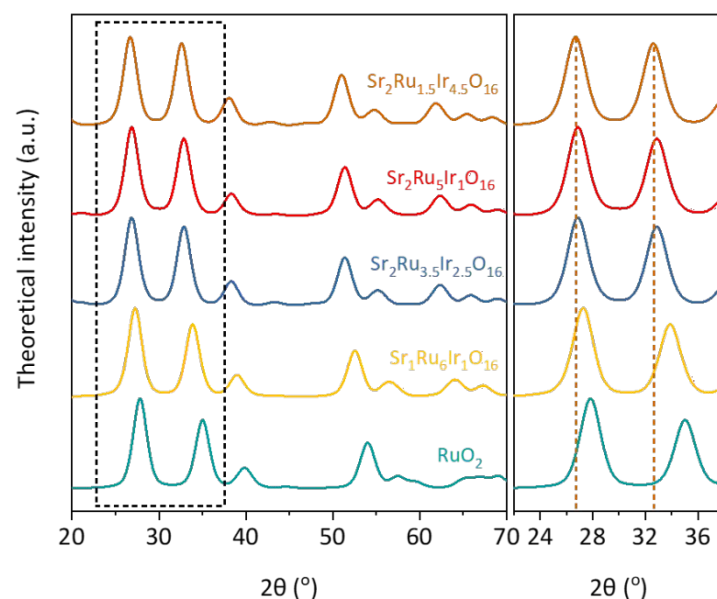
2 **Supplementary Figure 2 | Simulated XRD patterns from the DFT models.** Crystal

3 sizes of 50 nm × 50 nm × 50 nm are used to calculate peak broadening. The dot lines

4 at 27° and 33° represent (110) and (101) diffraction of rutile, respectively.

5

6
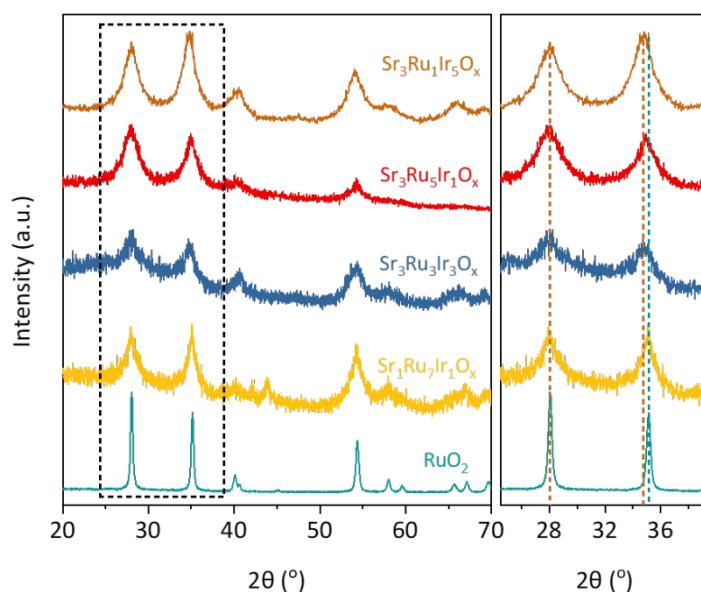
7 **Supplementary Figure 3 | XRD patterns of a series of Sr-Ru-Ir ternary oxide**

8 **catalysts.** Note that the Sr-Ru-Ir ratios are the feed ratios during catalyst synthesis. The

9 dot lines at 28° and 35° represent (110) and (101) diffraction of rutile, respectively.

10
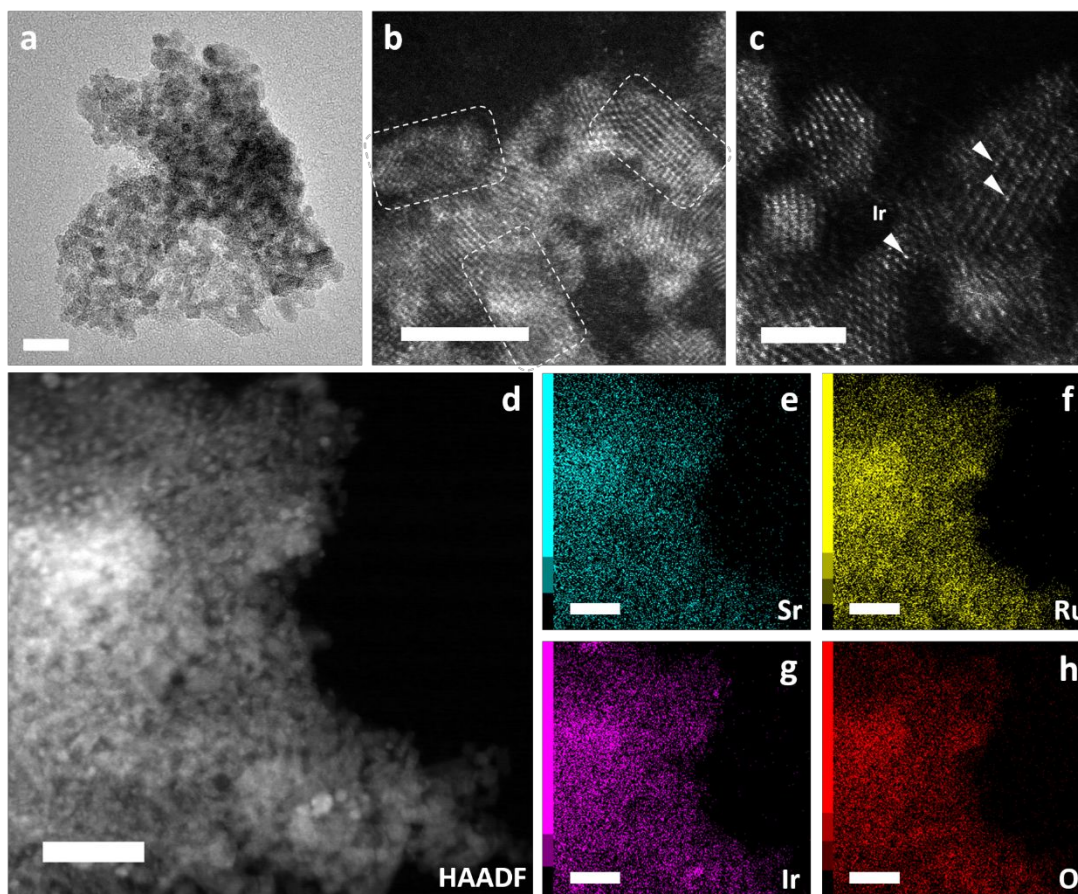
Supplementary Figure 4 | Morphology of as-prepared SrRuIr oxide catalysts. (a)
HR-TEM image of SrRuIr. Scale bar: 10 nm. **(b-c)** Atomic resolution HAADF-STEM
image of SrRuIr. Scale bar: 5 nm for **b** and 2 nm for **c**. The bright spot in the lattice can
be assigned to Ir dopants. Note that some oxide particles were reduced to metallic Ru
(or Ir) due to beam damage. **(d-h)** HAADF-STEM image and corresponding EDX
elemental mapping.
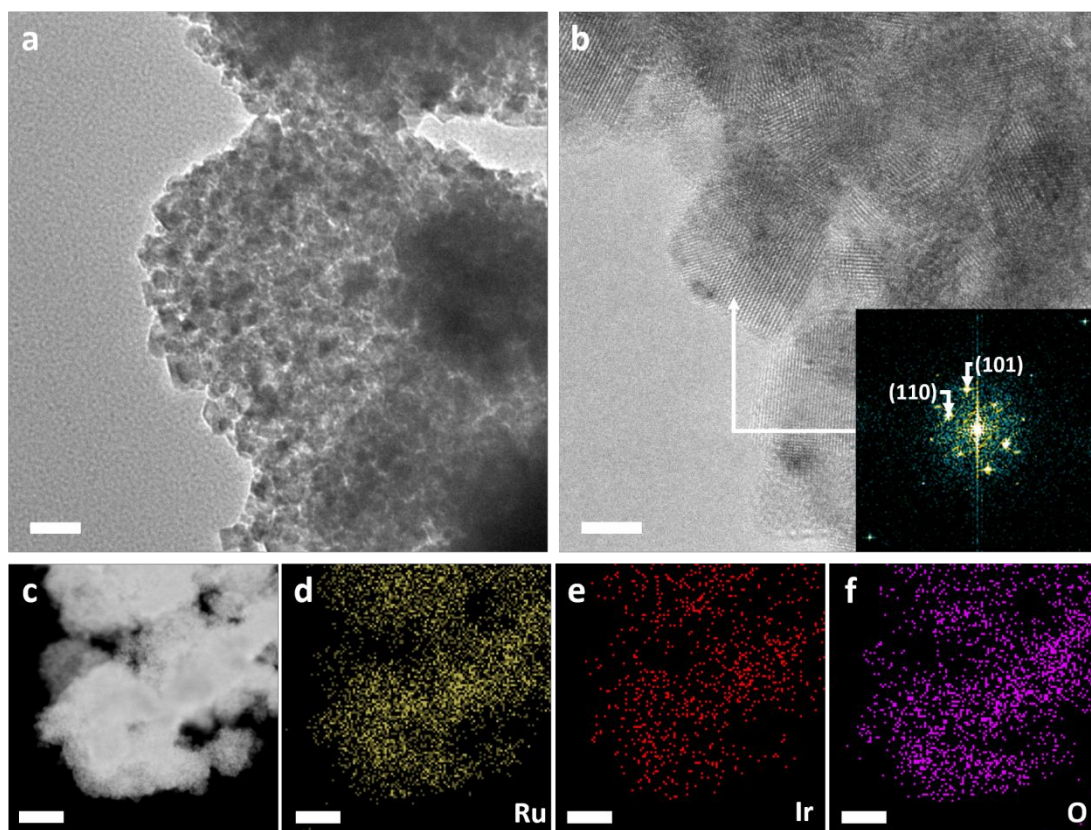
Supplementary Figure 5 | The TEM images RuIr oxide catalysts. (a) The TEM image of RuIr oxide. Scale bar: 20 nm. **(b)** The HR-TEM image of RuIr. Inset: The fast Fourier transformed (FFT) pattern from the nanoparticle can be indexed to (110) and (101) plane of rutile structure. Scale bar: 5 nm **(c-f)** HAADF-STEM image and corresponding EDX elemental mapping indicated a homogeneous dispersion of Ru Ir and O. Scale bar: 100 nm.

1
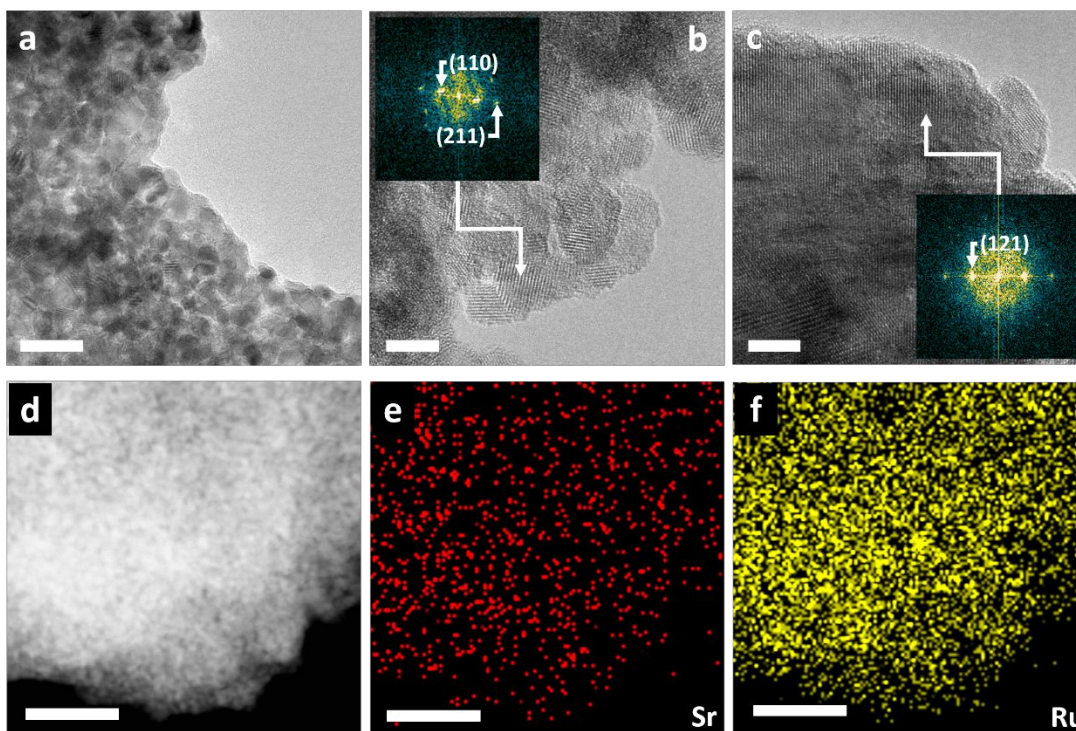
2 **Supplementary Figure 6 | The TEM images of SrRu oxide catalysts. (a)** The TEM

3 image of SrRu oxide. Scale bar: 20 nm. **(b)** The HRTEM image of rutile part. Inset:

4 The FFT pattern from the nanoparticle can be indexed to (110) and (211) planes of

5 rutile structure. Scale bar: 5 nm **(c)** The HRTEM image of perovskite part. Inset: Scale

6 bar: 5 nm. **(d-f)** HAADF-STEM image and corresponding EDX elemental mapping

7 indicating a homogeneous dispersion of Sr and Ru. Scale bar: 50 nm.

8

9
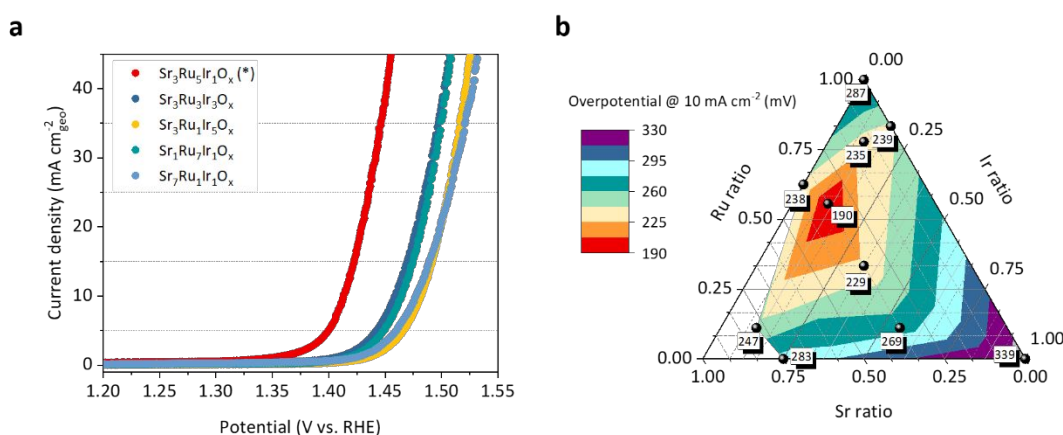
10 **Supplementary Figure 7 | OER polarization curves of Sr-Ru-Ir catalysts with**

11 **different ratios. (a)** The OER polarization curves of representative ternary catalysts.

12 The marked (*) feed ratio was denoted SrRuIr in the main text. **(b)** Summary of the

13 overpotential of different catalysts. Measured at 10 mV s^{-1} scan rate, with 95% iR-

14 compensation.

15

1
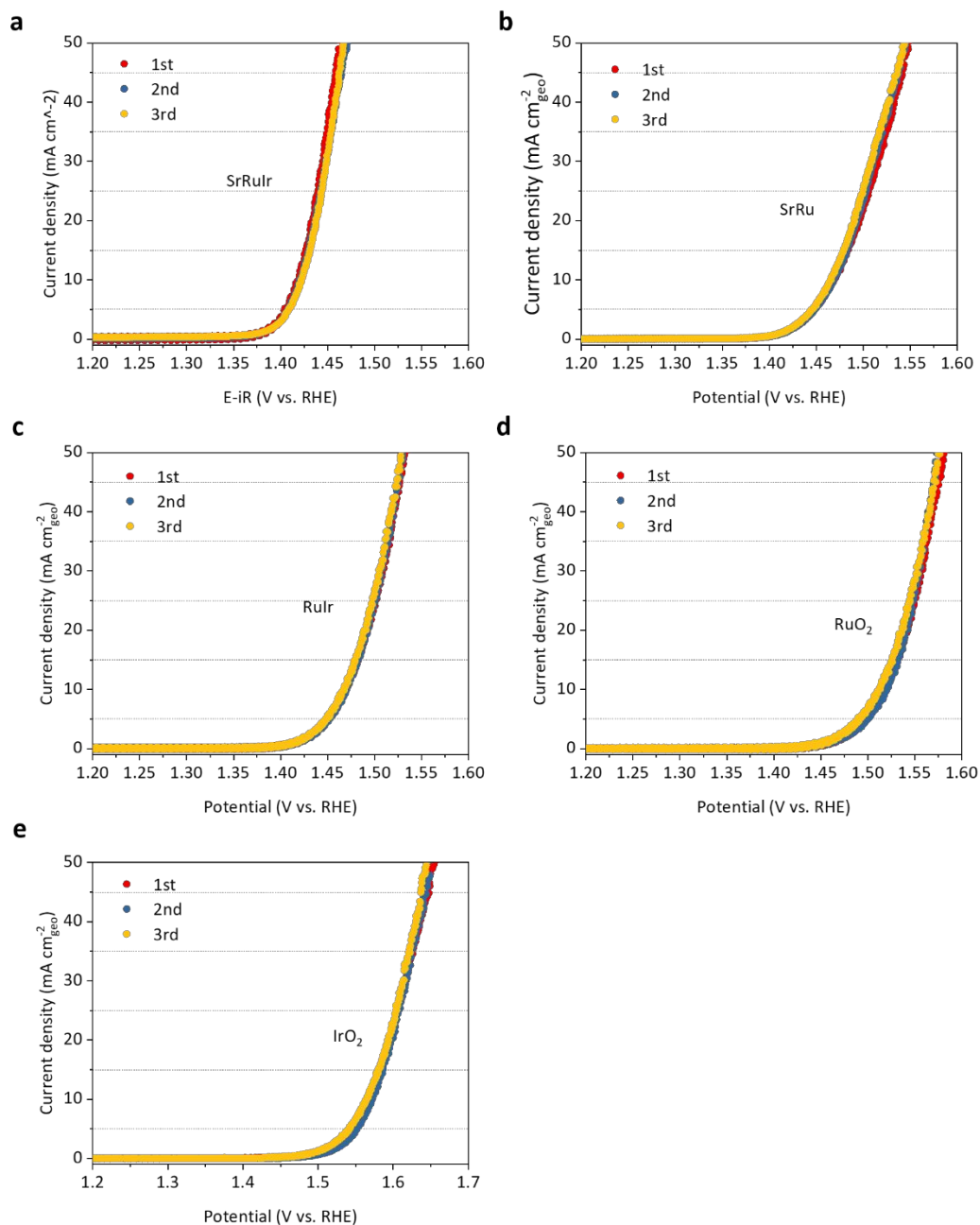
2 **Supplementary Figure 8 | Repeatability of linear sweep voltammetry (LSV) scans**

3 **for different catalysts.** (**a**) SrRuIr, (**b**) SrRu, (**c**) RuIr, (**d**) RuO_2 and (**e**) IrO_2. Measured

4 on GCE. Scan rate: 10 mV s^{-1}, with 95% iR-compensation. At least three independent

5 scans were carried out on different catalysts. The average overpotential at 10 mA cm^{-2}

6 was reported in the main text.

7

1
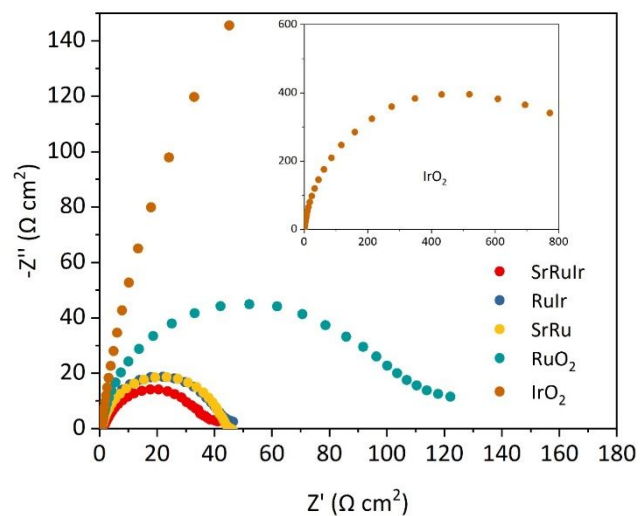
2 **Supplementary Figure 9 | EIS spectra of different catalysts.** Measured at 1.40 V *vs.*

3 RHE. Inset: Full range spectrum of IrO_2.

4

5
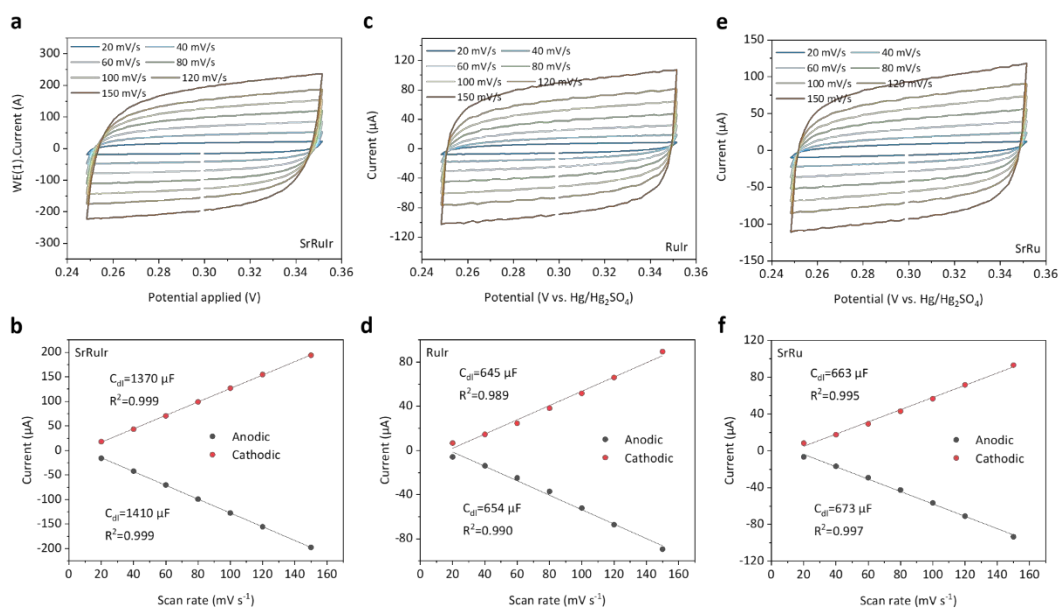
6 **Supplementary Figure 10 | The measurement of C_{dl} on different catalysts.** The

7 ECSA for each electrode is **(a-b)** 39.7 cm^2 for SrRuIr. **(c-d)** 18.6 cm^2 for RuIr. **(c-d)**

8 19.1 cm^2 for SrRu. A specific capacitance of 35 $\mu F\ cm^{-2}$ was used in the calculations.

9
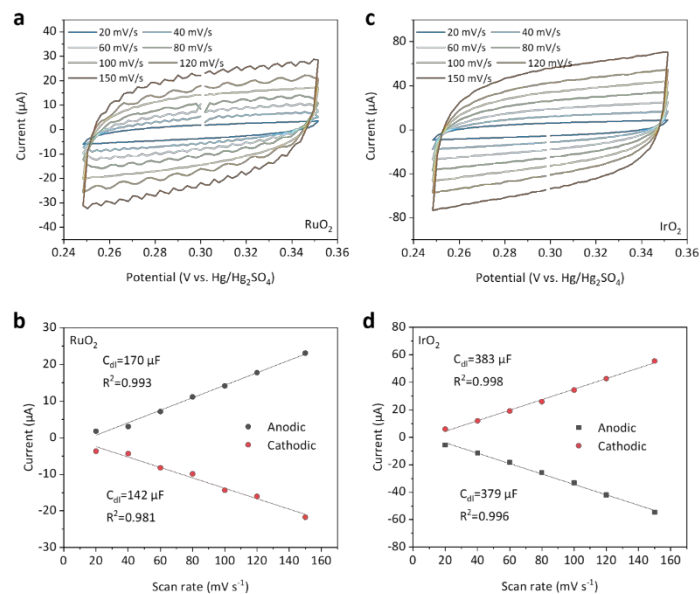
Supplementary Figure 11 | The measurement of C_{dl} on commercial catalysts. The ECSA for each electrode is **(a-b)** 10.9 cm^2 for IrO$_2$. **(c-d)** 4.4 cm^2 for RuO$_2$. A specific capacitance of 35 µF cm^{-2} was used in the calculations.
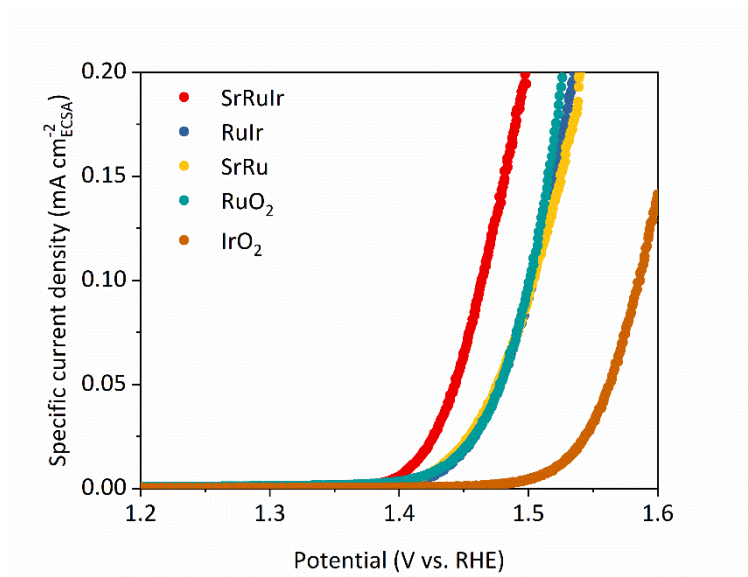

Supplementary Figure 12 | LSV curves normalized by ECSA of different catalysts. The ECSA values were obtained from the double layer capacitance (C_{dl}). The C_{dl} values were measured by conducting CV cycles at non-Faradic potential range at different scan rate.

1
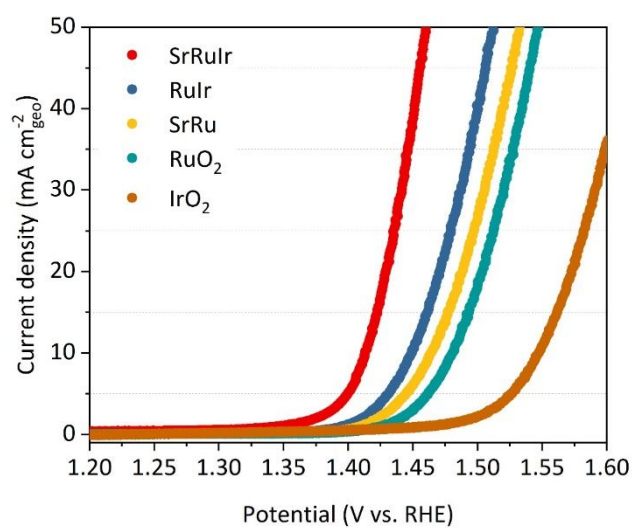
Supplementary Figure 13 | OER polarization curves of different catalyst measured on carbon paper. Measured at 10 mV s^{-1} scan rate, iR compensated and capacitive current corrected.

5

6
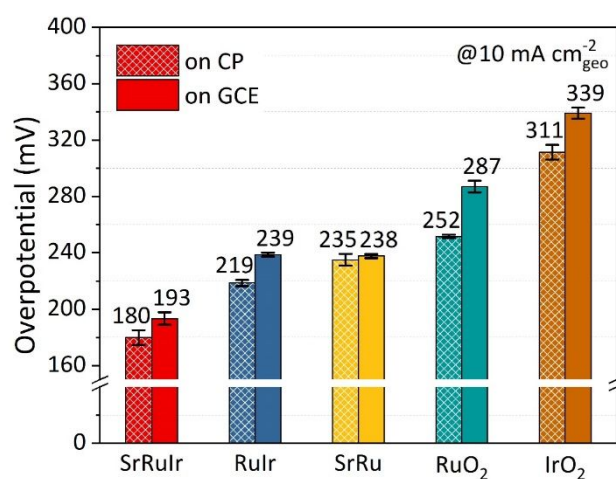
7 **Supplementary Figure 14 | Summary of overpotential at 10 mA cm$^{-2}_{geo}$ on different**
8 **catalysts.**

9
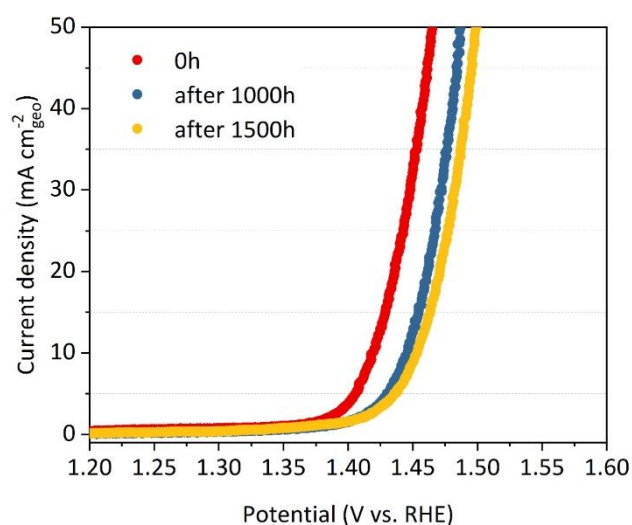
1
2 **Supplementary Figure 15 | OER polarization curves of SrRuIr after long-term**
3 **operation.**
4
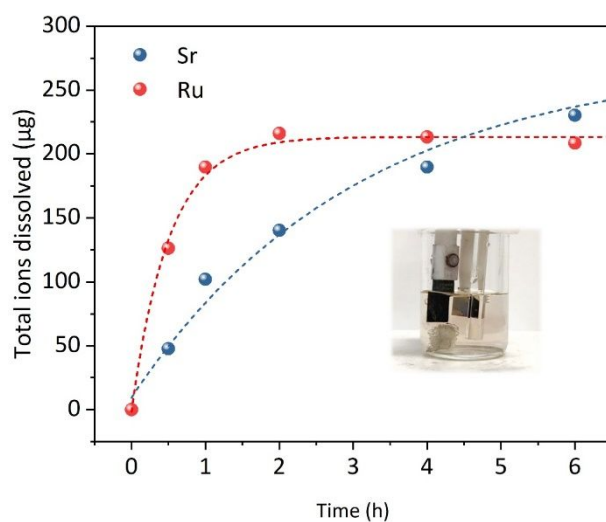
5
6 **Supplementary Figure 16 | Ion dissolution of SrRu oxide.** Both Sr and Ru were
7 leaching rapidly in SrRu. The solution even turned to brownish red after electrolysis,
8 indicating the formation and dissolution of high-valence Ru species (likely RuO_4^{2-})[14].
9 A low volume of electrolyte was used to (1) increase the concentration of ions for better
10 ICP-OES sensitivities and (2) make the color change of the electrolyte clearer.
11

1
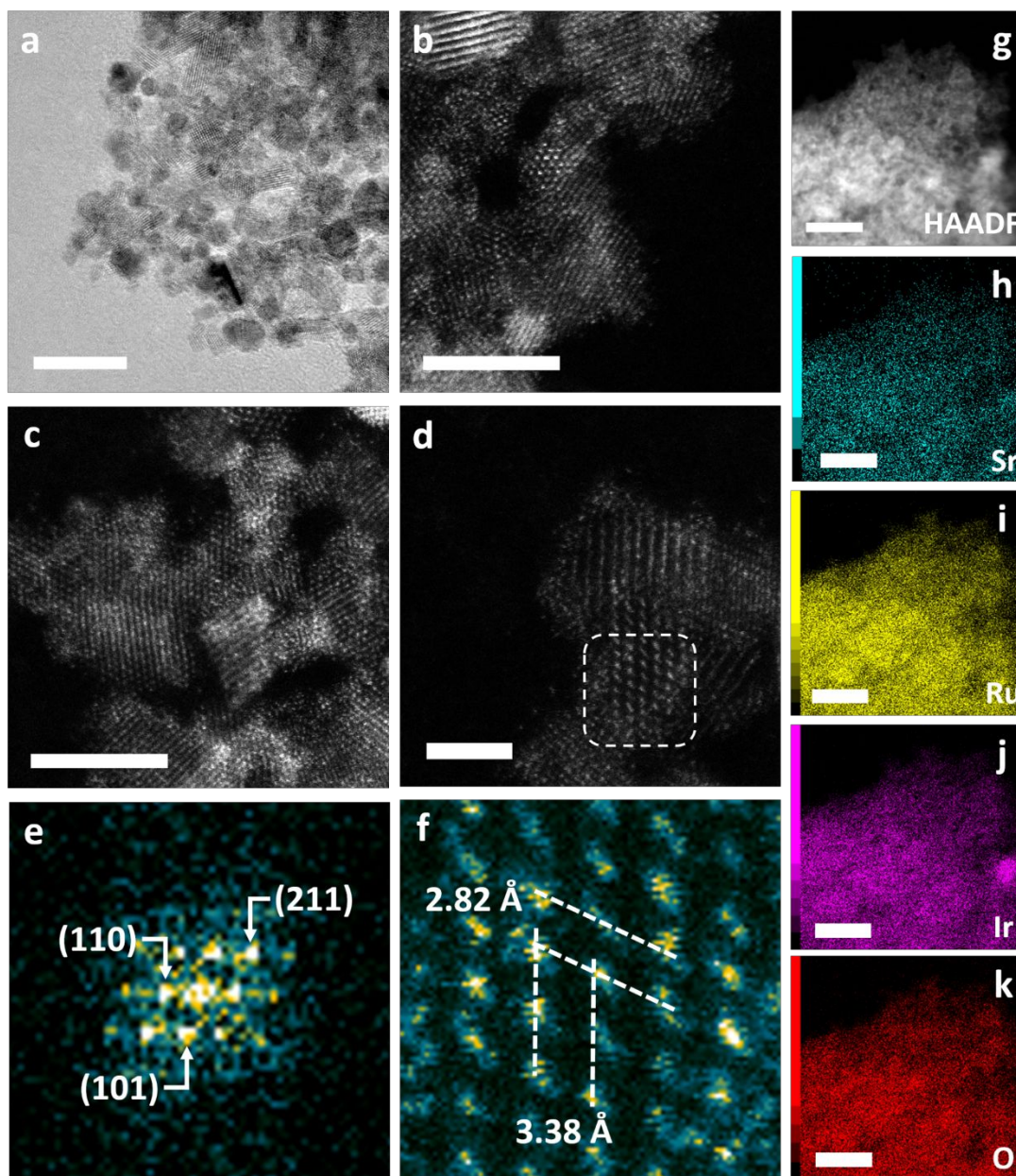
2 **Supplementary Figure 17 | TEM study of SrRuIr catalysts after 24 h OER. (a)** The

3 high-resolution TEM image of SrRuIr. Scale bar: 10 nm **(b-d)** Atomic resolution

4 HAADF-STEM image of SrRuIr. Scale bar: 5 nm for **b**, **c** and 2 nm for **d**. Note that

5 some oxide particles were reduced to metallic Ru (or Ir) due to beam damage. **(e)** The

6 FFT of selected area in **d**. **(f)** The inverse FFT of **e**. The *d*-spacing were 3.38 Å and 2.82

7 Å for (110) and (101) plane, respectively. These values are larger than the pristine RuO_2

8 (3.18 Å and 2.56 Å), which can be ascribed to the incorporation of Sr and Ir. **(g-k)**

9 HAADF-STEM image and corresponding EDX elemental mapping. Scale bar: 20 nm.

10

1
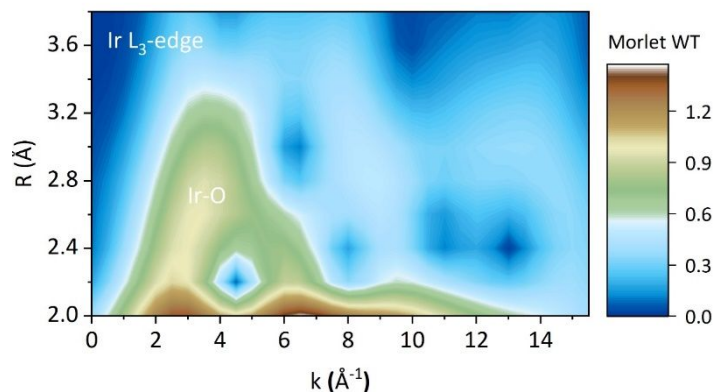
2 **Supplementary Figure 18 | WT-EXAFS of IrO$_2$.** The Morlet function parameter was

3 $\eta = 7.4$, $\sigma = 1$. In IrO$_2$, the peak at R≈3.2 Å, k≈8.5 Å^{-1} did not appear, indicating the

4 R≈3 Å, k≈8.5 Å^{-1} peak in SrRuIr came from Ru-Ir scattering.

5

6
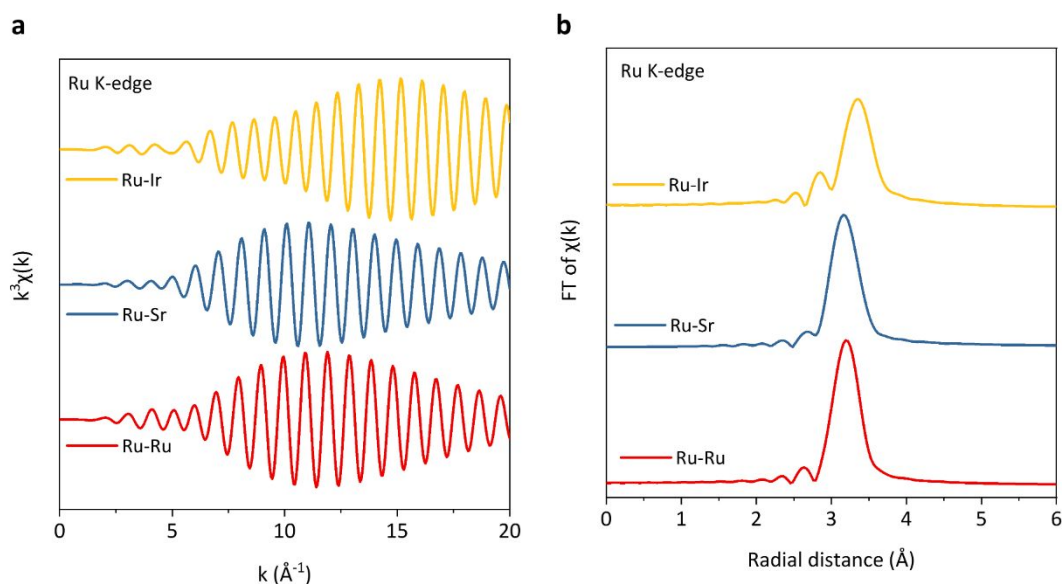
7 **Supplementary Figure 19 | EXAFS scattering paths of Ru-Ru, Ru-Sr, Ru-Ir**

8 **obtained by *ab initio* calculations.** (**a**) The scattering path in *k*-space. (**b**) The

9 scattering path in *R*-space. The maximum of Ru-Ru and Ru-Sr scattering path were

10 both located at k ≈ 11 Å^{-1}, R ≈ 3.2 Å. While Ru-Ir scattering path was located at k ≈ 15

11 Å^{-1}, R ≈ 3.5 Å. The difference between the maximum value of FT-EXAFS path and

12 WT-EXAFS is due to the k-weight factor[6].

13
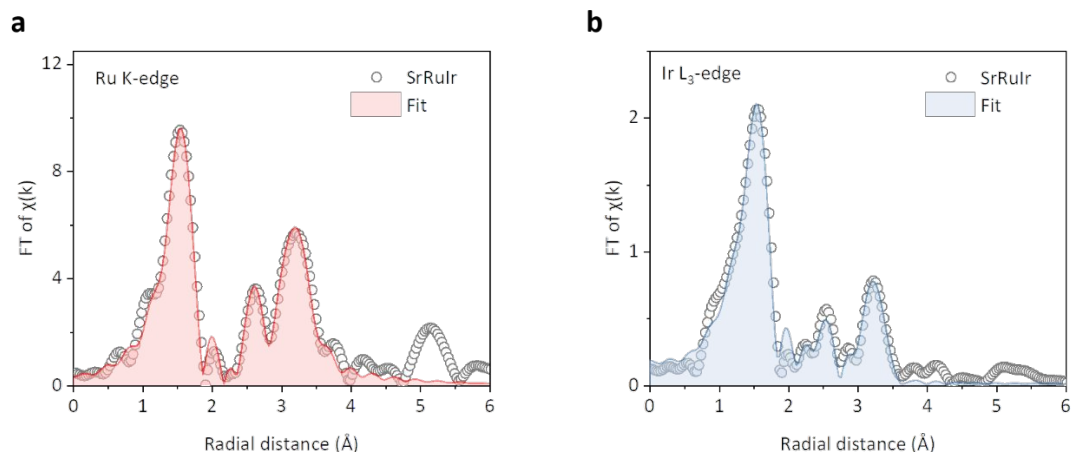
Supplementary Figure 20 | The EXAFS fitting of SrRuIr. (**a**) Ru K-edge (k weight=3). (**b**) Ir L_3-edge (k weight=2).
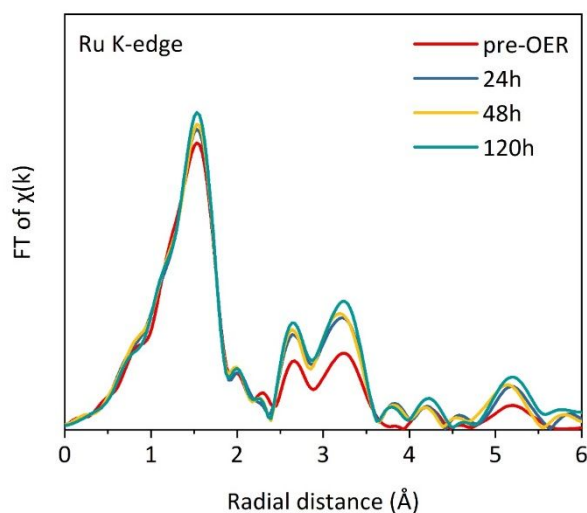
Supplementary Figure 21 | Ru K-edge FT-EXAFS spectra of SrRuIr after 24, 48, 120h electrolysis (k weight =2). During the long-term OER, the intensity of the peaks at larger radial distances increased slightly, indicating an increase in structural order over time. This structural change might be caused by the Sr leaching, which might be one of the reasons for the decrease in activity.
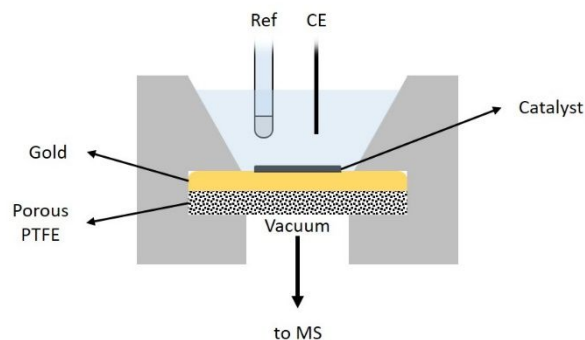
1
2 **Supplementary Figure 22 | The electrochemical cell configuration used in DEMS**
3 **measurements.**
4
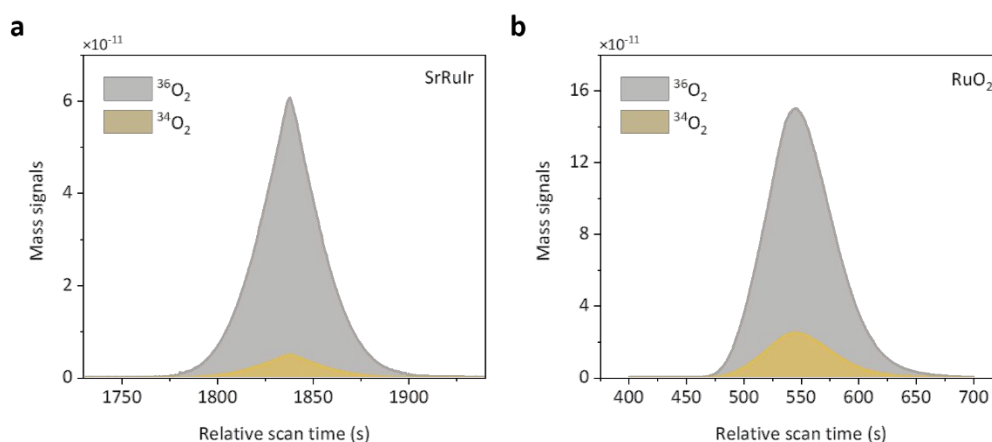
5
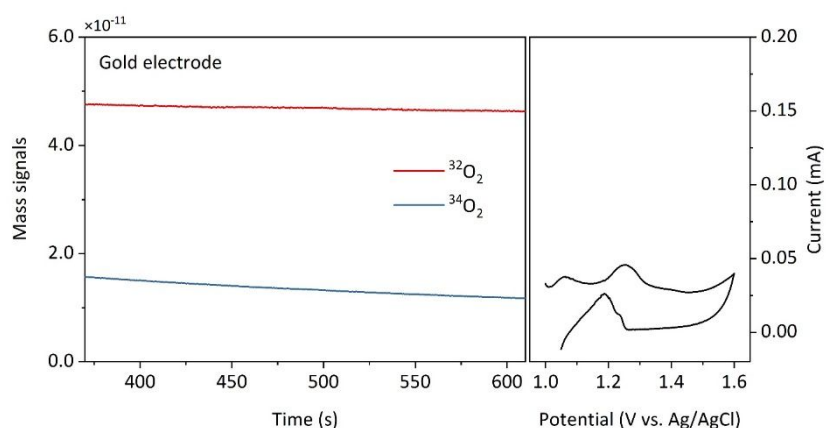6 **Supplementary Figure 23 | DEMS signals of $^{34}O_2$ and $^{36}O_2$ from the reaction**
7 **products cycled in $H_2^{18}O$ aqueous sulfuric acid electrolyte. (a)** SrRuIr; **(b)** RuO$_2$.
8 From the area ratio of $^{34}O_2$ and $^{36}O_2$, the amount of LOM can be quantified.
9

10
11 **Supplementary Figure 24 | The DEMS measurement on clean Au electrode.** No
12 $^{32}O_2$ or $^{34}O_2$ signal was observed under applied potential, which indicated that all $^{34}O_2$
13 signals measured were contributed by catalyst.
14
15

1
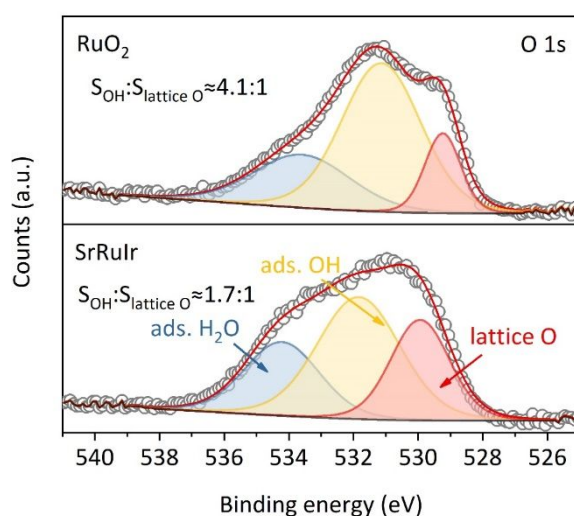
2 **Supplementary Figure 25 | The O 1s XPS spectra after 12h OER.** The area ratio
3 between adsorbed OH and lattice oxygen was much higher in RuO_2 than in SrRuIr,
4 which means the surface oxygen was more easily to be protonated in RuO_2, leading to
5 higher possibility to participate LOM. This find supported the results of DEMS.

6

7
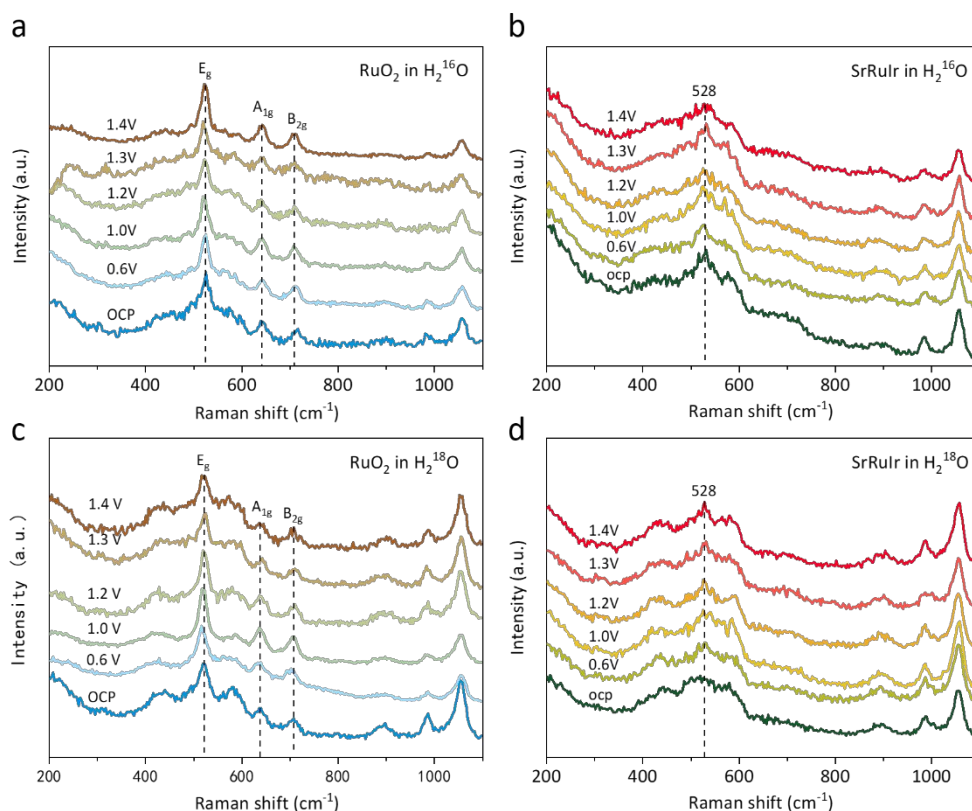
8 **Supplementary Figure 26 | The *in situ* Raman spectroscopy of SrRuIr and RuO_2.**
9 **(a-b)** Spectra in ordinary 0.5 M H_2SO_4. **(c-d)** Spectra in $H_2^{18}O$ labeled 0.5 M H_2SO_4.

1   Note that the peak at 435 cm^{-1}, 580 cm^{-1} and 895 cm^{-1} came from the oxidation of Ti

2   substrate. The peak at 985 cm^{-1} and 1055 cm^{-1} came from SO$_4^{2-}$.

3
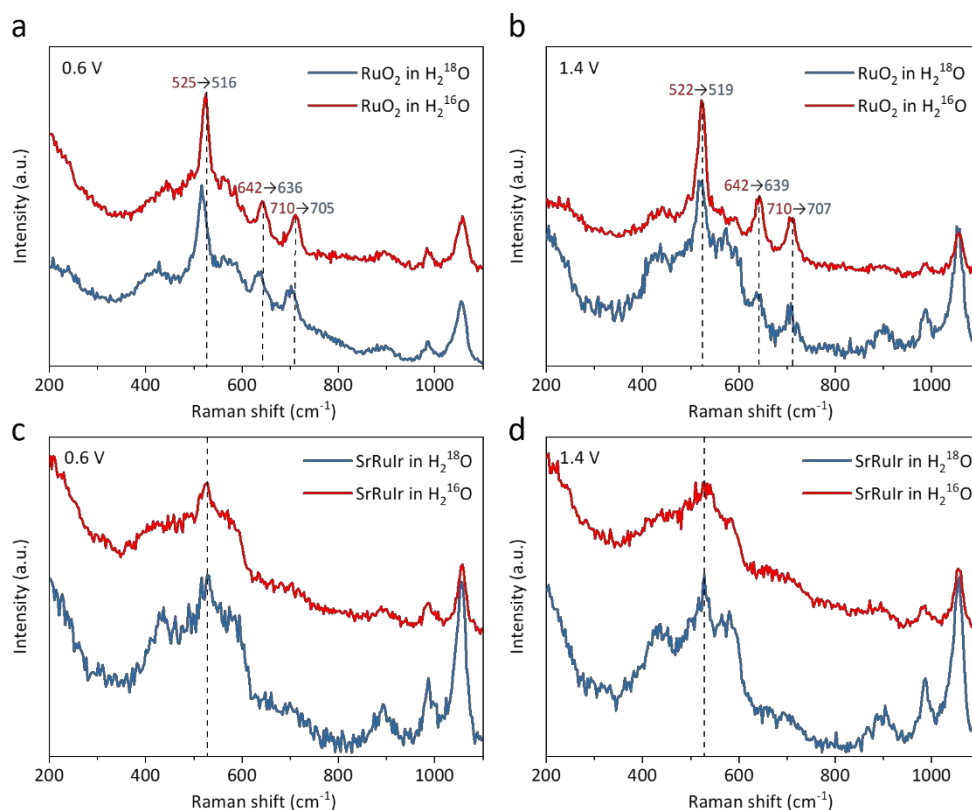
4
5   **Supplementary Figure 27 | The *in situ* Raman spectra of SrRuIr and RuO$_2$. (a &**
6   **c)** RuO$_2$ at 0.6 V and 1.4 V vs. RHE, respectively. **(b & d)** SrRuIr at 0.6 V and 1.4 V
7   vs. RHE, respectively. Note that the peak at 435 cm^{-1}, 580 cm^{-1} and 895 cm^{-1} came from
8   the oxidation of Ti substrate. The peak at 985 cm^{-1} and 1055 cm^{-1} came from SO$_4^{2-}$.

9

a

AEM

$* \, OOH \rightarrow * \, O_{2(g)} + e^- + H^+$

$* \, O + H_2O \rightarrow * \, OOH + e^- + H^+$

*OOH

$* + H_2O \rightarrow * \, OH + e^- + H^+$

$* \, OH \rightarrow * \, O + e^- + H^+$

*

*OH

*O

LOM

$* \, H \rightarrow * + e^- + H^+$

$* \, O + O_{lattice} \rightarrow * \, O_{2(g)} + V_O$
(non-electrochemical step)

$V_O + H_2O \rightarrow * \, H + e^- + H^+$

*H$_{O\text{-site}}$

c

Sr$_2$Ru$_5$Ir$_1$O$_{16}$

η_{AEM} = 0.21 V
η_{LOM} = 1.22 V

Free energy ΔG (eV)

*H$_{O\text{-site}}$

2.45 eV

1.40 eV

1.44 eV (PDS)

1.33 eV

0.75 eV

* + H$_2$O   *OH   *O   *OOH   * + O$_2$

Reaction Coordinates

b

Sr$_1$Ru$_6$Ir$_1$O$_{16}$

η_{AEM} = 0.37 V
η_{LOM} = 1.69 V

Free energy ΔG (eV)

*H$_{O\text{-site}}$

2.92 eV

1.51 eV

1.60 eV (PDS)

1.34 eV

0.47 eV

* + H$_2$O   *OH   *O   *OOH   * + O$_2$

Reaction Coordinates
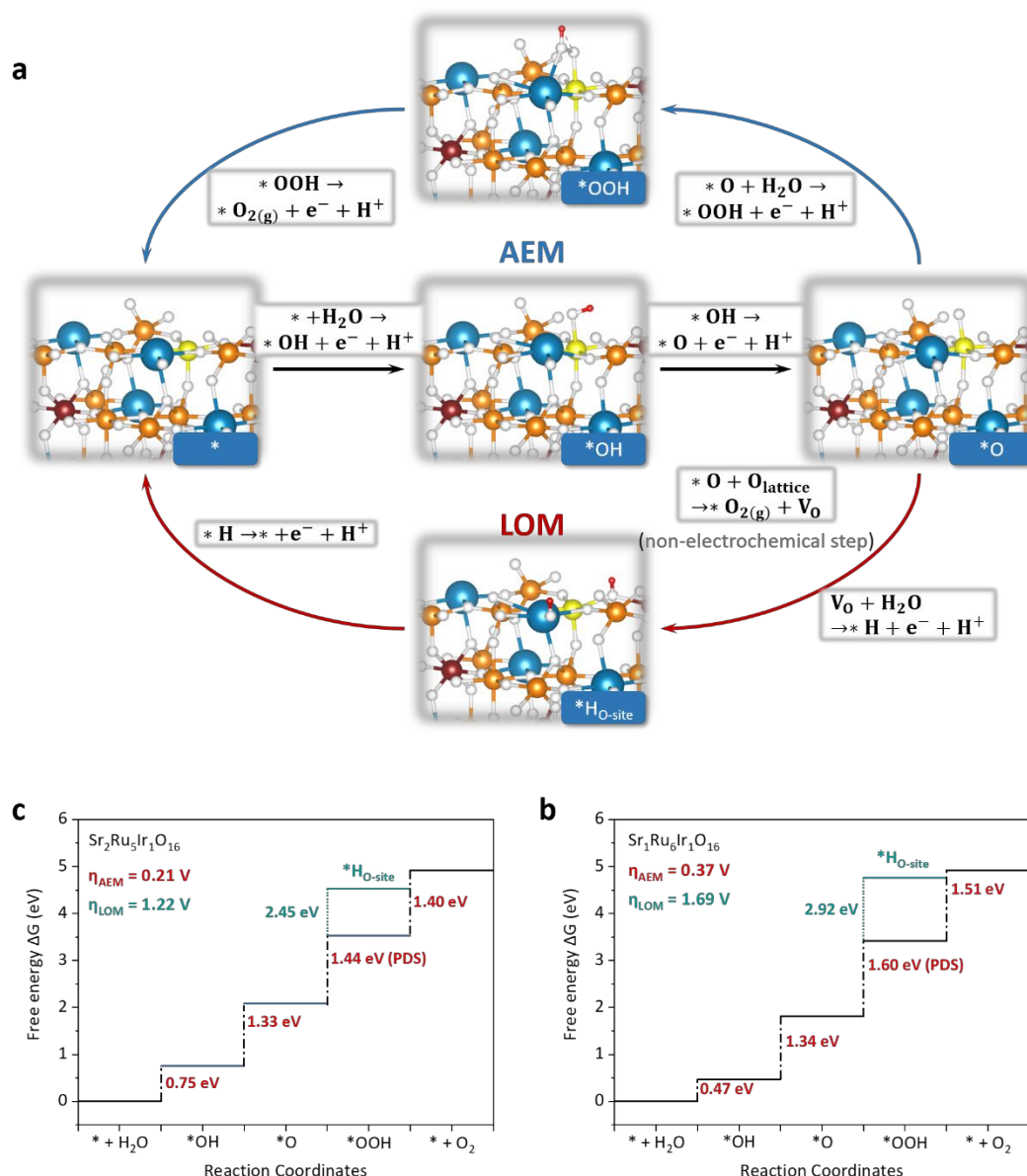
Supplementary Figure 28 | Different OER pathways on SrRuIr oxide catalysts. (a) The schematics of OER pathways. The LOM pathway is refer to ref.[15]. **(b)** The OER energetics of Sr$_2$Ru$_5$Ir$_1$O$_{16}$. **(c)** The OER energetics of Sr$_1$Ru$_6$Ir$_1$O$_{16}$. The overpotential of LOM pathway is much higher than the AEM pathway on both models. While with the decrease of Sr, the overpotential of LOM increased accordingly. This result well coincide with our experiment that the catalyst is getting stable after Sr leaching.

1
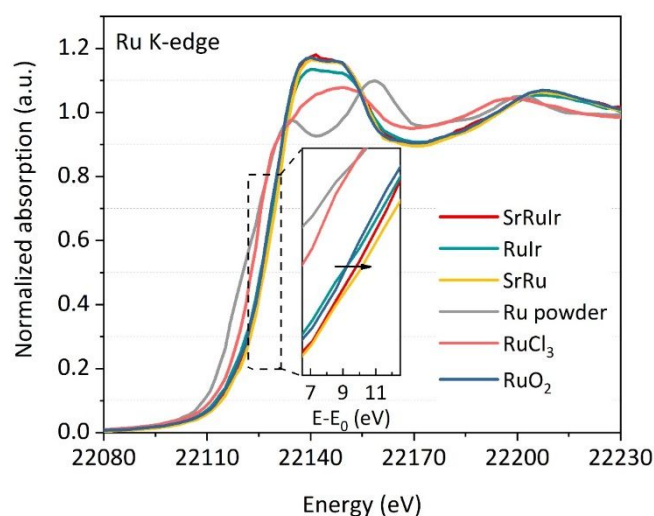
2 **Supplementary Figure 29 | *In-situ* Ru K-edge XANES of different catalysts.** The
3 XANES measurements were conducted at 1.35 V *vs*. RHE. The absorption edge of both
4 SrRuIr and SrRu moved to higher energy, indicating a Ru valence of Ru^{n+} (n>4), while
5 the Sr-free RuIr oxide was kept as Ru^{4+}, the same as RuO_2 standard.

6

7
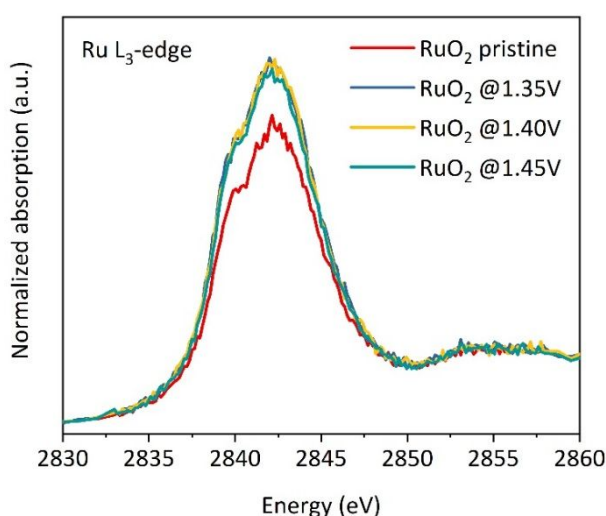
8 **Supplementary Figure 30 | The *in situ* Ru L_3-edge XAS spectra of RuO_2.** The white-
9 line peak did not vary significantly under different potential.

10

1
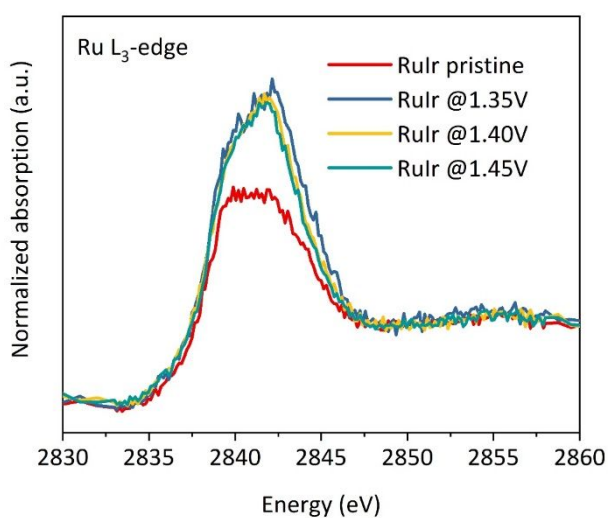
2 **Supplementary Figure 31 | The *in situ* Ru L₃-edge XAS spectra of RuIr.** The white-

3 line peak did not vary significantly with various applied potentials.

4

5
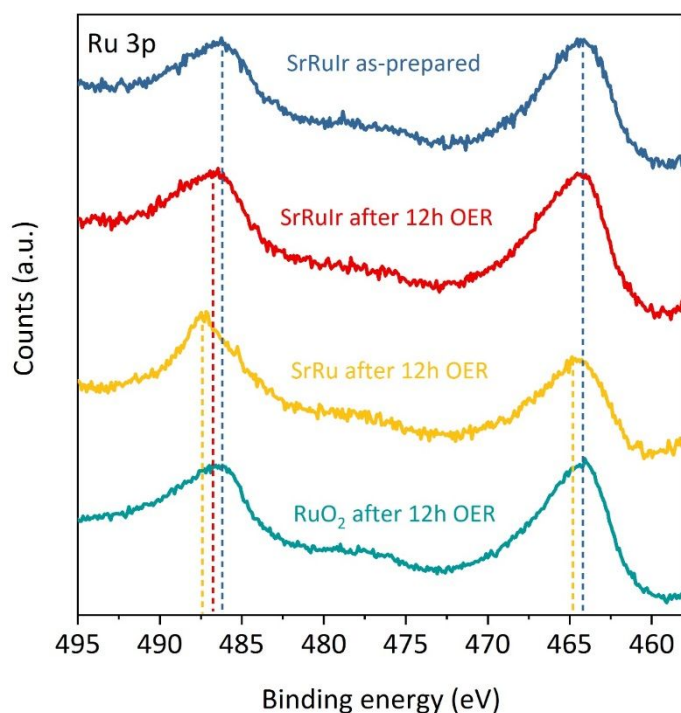
6 **Supplementary Figure 32 | The XPS spectra of Ru 3p for different catalysts.** The

7 chemical state of Ru in as-prepared SrRuIr is +4, same with RuO_2. After 12-h -

8 electrolysis, a shoulder arise at *ca.* 487 eV, which hinted the formation of Ru^{n+} (n>+4)

9 surface species.

10

Sr3Ru5O16
PDOS (States·eV-1·Ru-1)
40
30
20
10
0
t2g
eg
d band
-10
-8
-6
-4
-2
0
2
4
6
8
E-EFermi (eV)
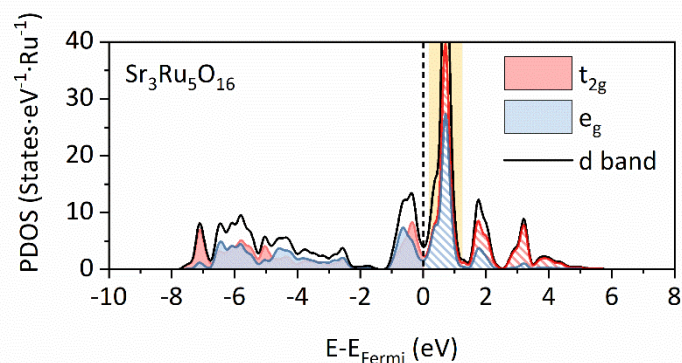
Supplementary Figure 33 | PDOS of the active Ru site on $Sr_3Ru_5O_{16}$ model. The incorporation of Sr induced more unoccupied e_g state at ~ 1 eV above Fermi level.

Ir 4f
SrRuIr
as-prepared
after 12h OER
IrO2 ref.
Counts (a.u.)
74
72
70
68
66
64
62
60
58
Binding energy (eV)
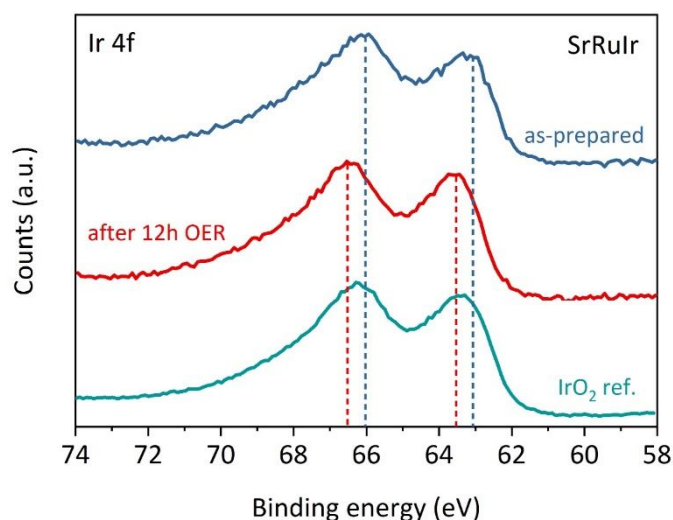
Supplementary Figure 34 | The XPS spectra of Ir 4f for SrRuIr catalyst before and after OER. The Ir in pristine catalyst showed a valence of +3. After performing 12-h continuous electrolysis, the Ir was oxidized to chemical state even higher than IrO_2 (+4).
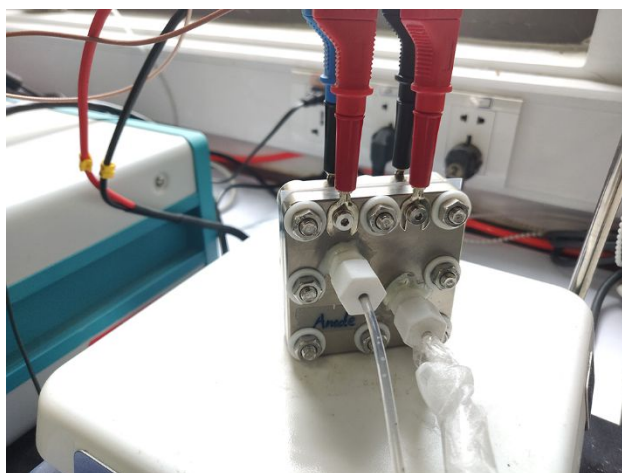
1
2   **Supplementary Figure 35 | Photograph of the PEM set-up used in this work.**
3
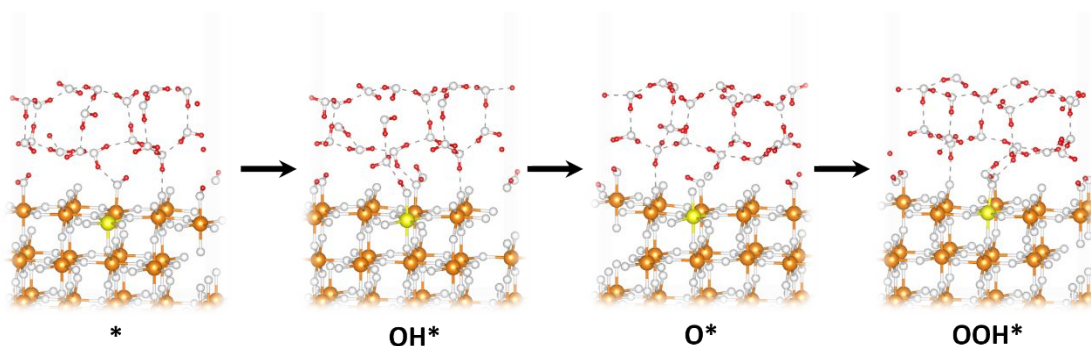
4
5   **Supplementary Figure 36 | The OER pathway of RuO$_2$ on explicit solvent models.**
6   The orange balls represent Ru atoms, and the small red and white balls are hydrogen
7   and oxygen atoms, respectively. The active sites are labeled as yellow.
8

1
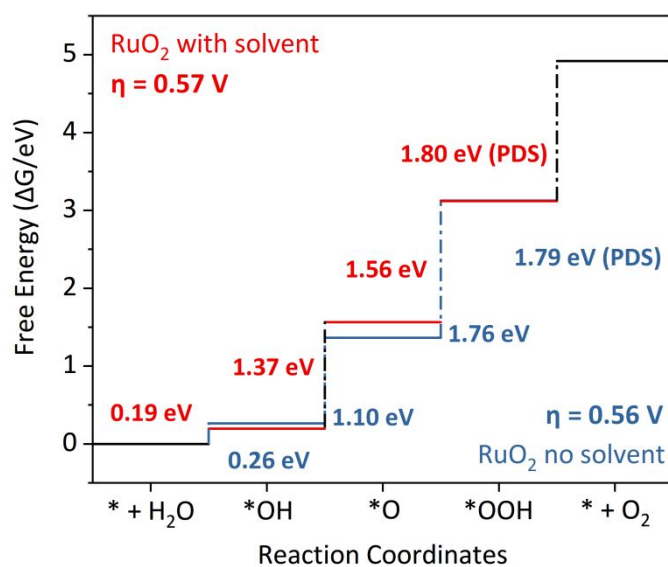
Supplementary Figure 37 | The comparison of reaction coordinates between models with and without solvent. No significant change was observed after including solvent. PDS is the potential determine step.

5

Sr$_1$Ru$_6$Ir$_1$O$_{16}$	Sr$_2$Ru$_{5.5}$Ir$_{0.5}$O$_{16}$	Sr$_3$Ru$_4$Ir$_1$O$_{16}$
E$_{total}$ = -343.53 eV	E$_{total}$ = -334.65 eV	E$_{total}$ = -324.50 eV

6
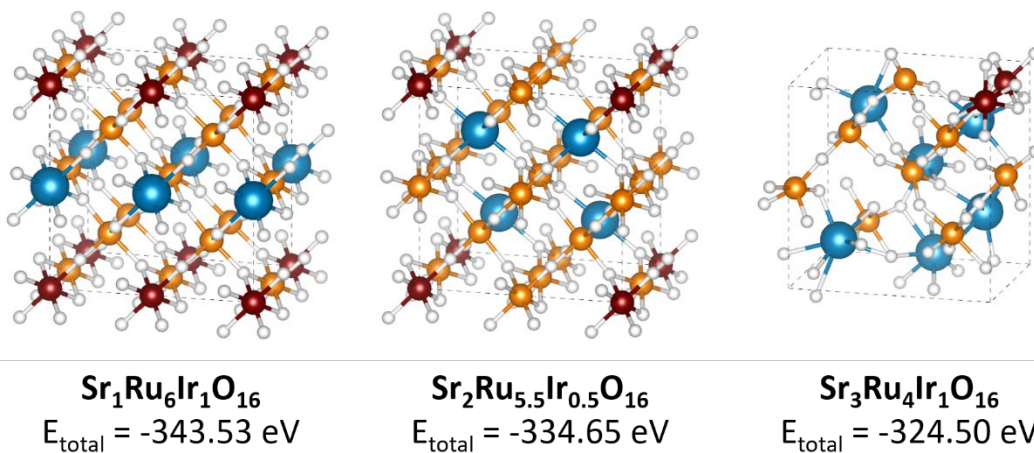
Supplementary Figure 38 | The structures and total energy of Sr-Ru-Ir crystals with different content of Sr doping.

9

1
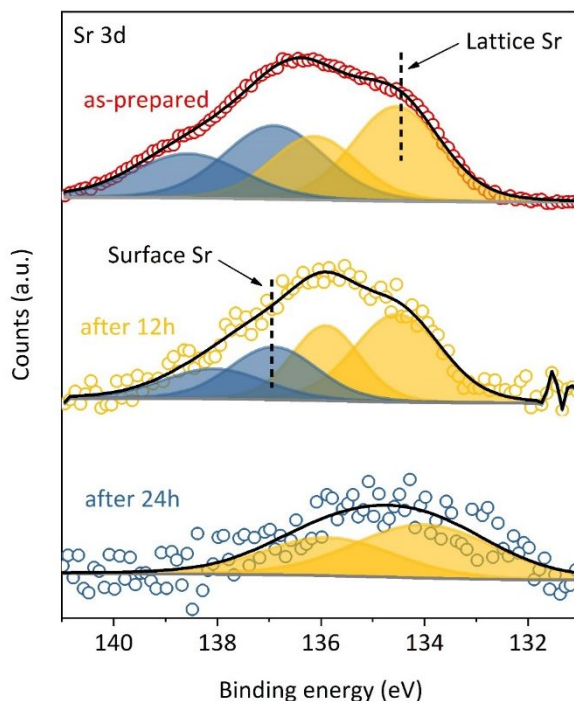
2 **Supplementary Figure 39 | Sr 3d XPS spectra of SrRuIr.** The results showed that

3 surface Sr were leached and the rest lattice Sr were stable during OER.

4

5
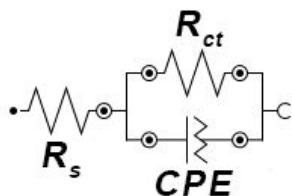
6 **Supplementary Figure 40 | Equivalence circuit used in electrochemical impedance**

7 **spectroscopy (EIS) fits.** R_s refers to the uncompensated resistance of electrolyte. R_{ct}

8 refers to the charge-transfer resistance. CPE refers to the constant phase element.

9
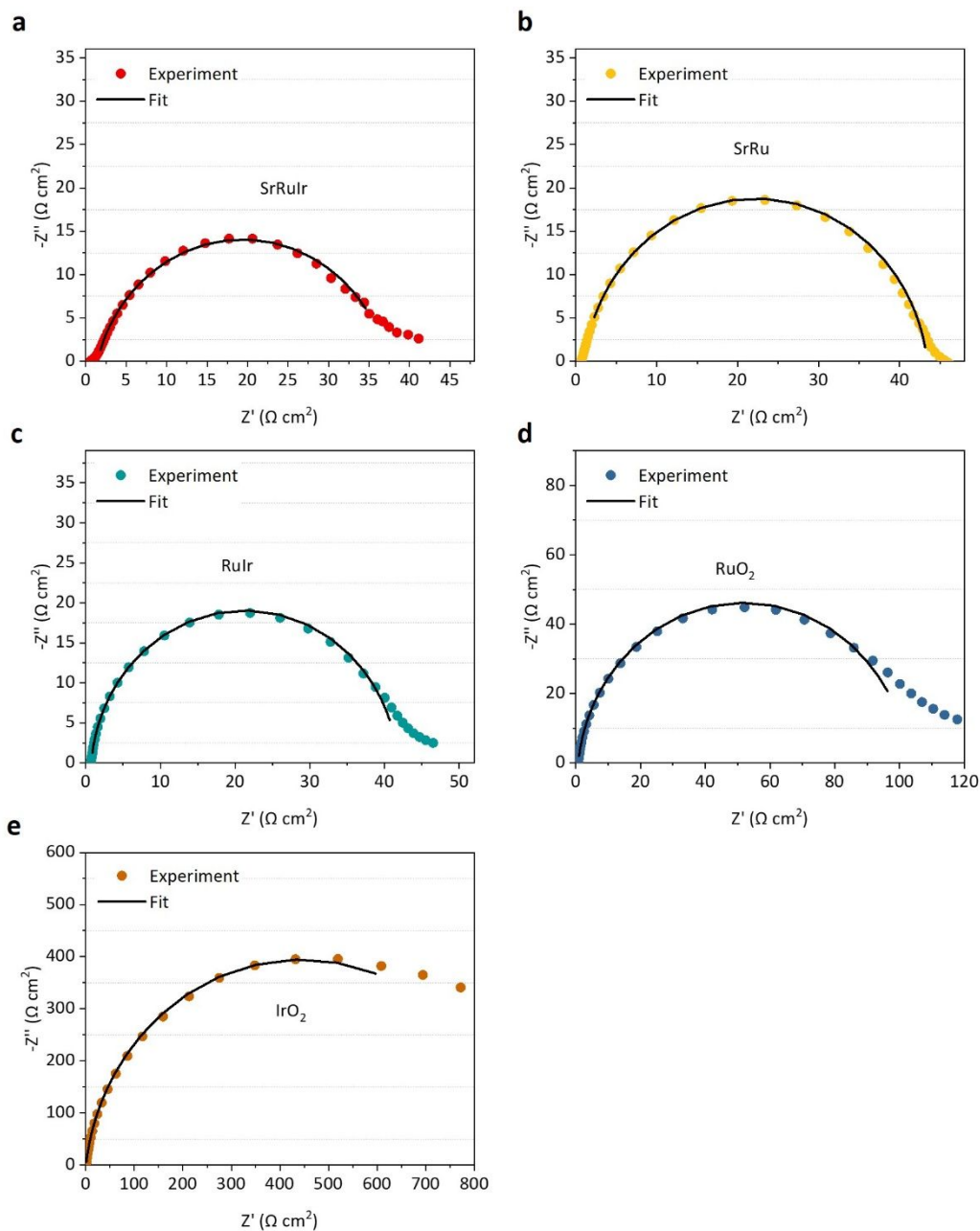
Supplementary Figure 41 | EIS spectrum and corresponding fit of different catalysts. (**a**) SrRuIr, (**b**) SrRu, (**c**) RuIr, (**d**) RuO_2 and (**e**) IrO_2. Measured on GCE at 1.35 V *vs.* RHE. The fitting parameters are summarized in **Supplementary Table 15**.
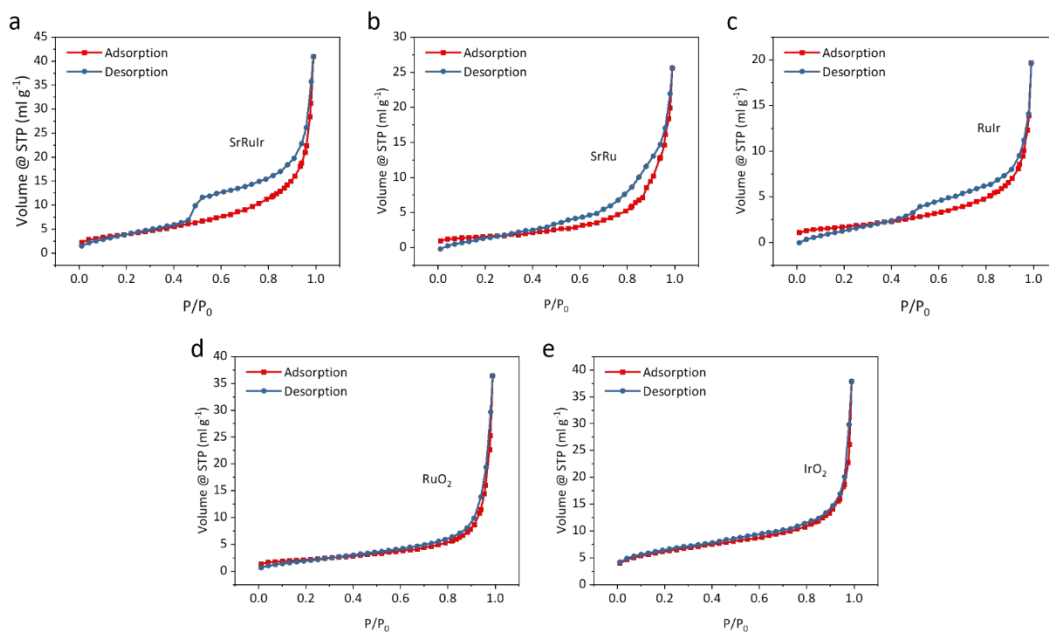
Supplementary Figure 42 | BET isotherms of different catalysts. (a) SrRuIr, (b) SrRu, (c) RuIr, (d) RuO_2 and (e) IrO_2.
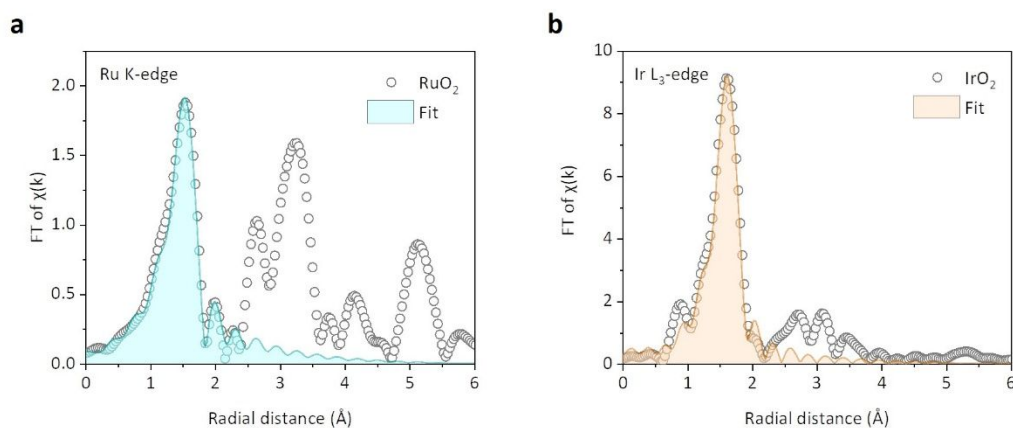
Supplementary Figure 43 | Firset shell EXAFS fitting of RuO_2 and IrO_2. (a) Ru K-edge of RuO_2 (k weight=2). (b) Ir L_3-edge of IrO_2 (k weight=3).

1
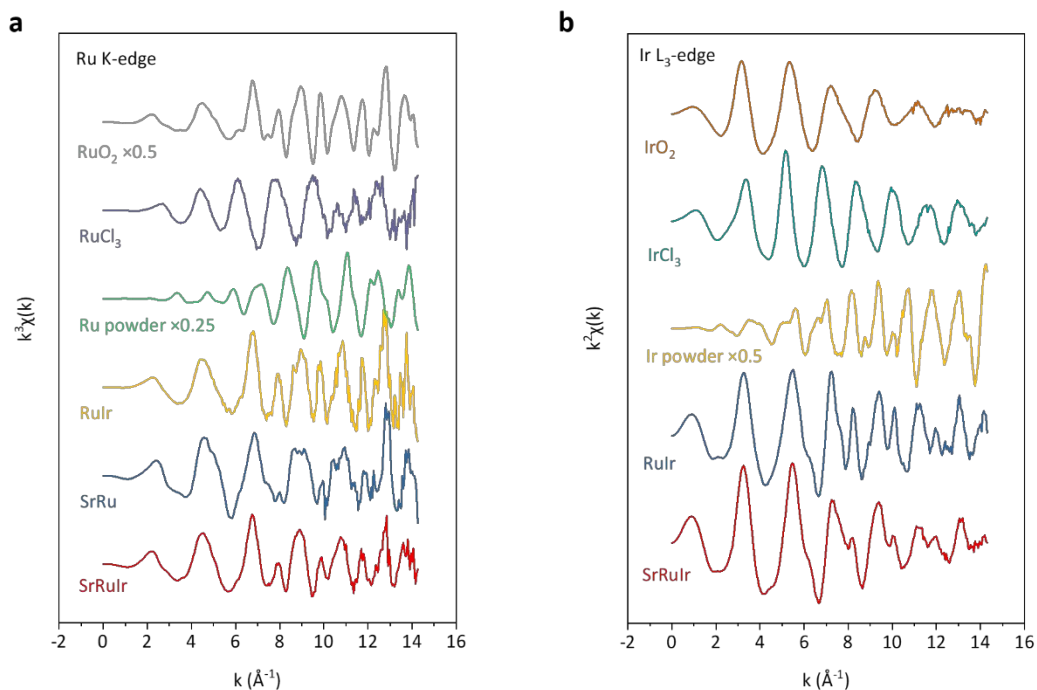
2 **Supplementary Figure 44 | EXAFS spectra of different samples in k space. (a)** Ru

3 K-edge. (**b**) Ir L_3-edge. All spectra possessed a low signal-to-noise ratio, indicating the

4 EXAFS measurements were reliable.

5

6
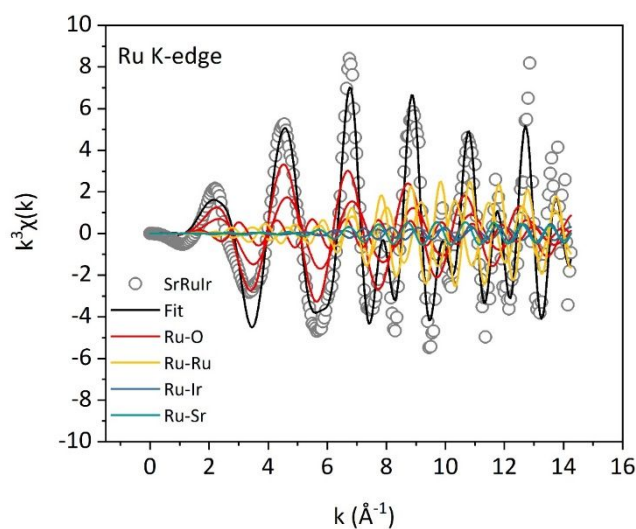
7 **Supplementary Figure 45 | Ru K-edge EXAFS spectra and corresponding fits of**

8 **SrRuIr.** K-weight = 3. The spectrum possessed a low signal-to-noise ratio and the R-

9 factor of fit was 0.0006, indicating the EXAFS measurements and fitting were reliable.

10

1
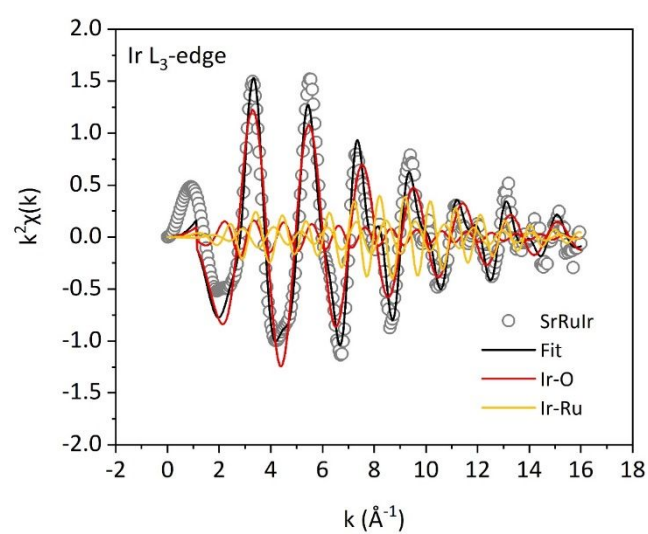
Supplementary Figure 46 | Ir L$_3$-edge EXAFS spectra and corresponding fits of SrRuIr. K-weight = 2. The spectrum possessed a low signal-to-noise ratio and the R-factor of fit was 0.0003, indicating the EXAFS measurements and fitting were reliable.

Supplementary Tables (Supplementary Table 1-Supplementary Table 15)

Supplementary Table 1 | DFT energies (eV), ΔZPE (eV) and TΔS (eV) for OER intermediates adsorbed on the different SrIrRuOx surface T=298.15K.

Model	Adsorbates	DFT energies	ΔZPE	TΔS
$Sr_1Ru_6Ir_1O_{16}$	*	-692.71	0	0
	*OH	-703.408	0.366	0.077
	*O	-698.339	0.071	0.057
	*OOH	-707.915	0.435	0.132
$Sr_2Ru_6O_{16}$	*	-680.42	0	0
	*OH	-690.848	0.364	0.079
	*O	-686.381	0.079	0.049
	*OOH	-695.646	0.439	0.125
$Sr_2Ru_{5.5}Ir_{0.5}O_{16}$	*	-678.257	0	0
	*OH	-688.65	0.361	0.081
	*O	-683.685	0.076	0.051
	*OOH	-693.28	0.444	0.181
$Sr_2Ru_5Ir_1O_{16}$	*	-675.819	0	0
	*OH	-686.224	0.357	0.087
	*O	-681.188	0.072	0.057
	*OOH	-690.878	0.442	0.182
$Sr_2Ru_{3.5}Ir_{2.5}O_{16}$	*	-669.256	0	0
	*OH	-679.853	0.365	0.078
	*O	-674.819	0.075	0.054
	*OOH	-684.364	0.439	0.131

	*	-659.240	0	0
Sr$_2$Ru$_{1.5}$Ir$_{4.5}$O$_{16}$	*OH	-669.791	0.362	0.082
	*O	-664.85	0.074	0.055
	*OOH	-674.367	0.440	0.131
	*	-663.099	0	0
Sr$_3$Ru$_5$O$_{16}$	*OH	-672.773	0.372	0.070
	*O	-667.567	0.079	0.039
	*OOH	-677.132	0.449	0.147
	*	-657.466	0	0
Sr$_3$Ru$_4$Ir$_1$O$_{16}$	*OH	-667.45	0.334	0.100
	*O	-662.227	0.074	0.045
	*OOH	-671.874	0.447	0.151
	*	-593.09	0	0
Sr$_6$Ru$_1$Ir$_1$O$_{16}$	*OH	-602.701	0.299	0.207
	*O	-597.813	0.071	0.062
	*OOH	-607.109	0.398	0.230
	*	-581.273	0	0
Sr$_6$Ir$_2$O$_{16}$	*OH	-591.854	0.373	0.053
	*O	-586.944	0.082	0.050
	*OOH	-596.577	0.472	0.131

1
2
3

1 **Supplementary Table 2 | Free energies for each OER reaction steps and the**
2 **calculated overpotential (η) on the SrRuIr surface.**

Model	ΔG_1	ΔG_2	ΔG_3	ΔG_4	η
$Sr_1Ru_6Ir_1O_{16}$	0.47	1.34	1.60	1.51	0.37
$Sr_2Ru_6O_{16}$	0.73	1.25	1.38	1.56	0.33
$Sr_2Ru_{5.5}Ir_{0.5}O_{16}$	0.77	1.26	1.53	1.36	0.30
$Sr_2Ru_5Ir_1O_{16}$	0.75	1.33	1.44	1.40	0.21
$Sr_2Ru_{3.5}Ir_{2.5}O_{16}$	0.57	1.32	1.63	1.40	0.40
$Sr_2Ru_{1.5}Ir_{4.5}O_{16}$	0.61	1.23	1.66	1.42	0.43
$Sr_3Ru_5O_{16}$	1.51	1.49	1.58	0.34	0.35
$Sr_3Ru_4Ir_1O_{16}$	1.13	1.57	1.50	0.72	0.34
$Sr_6Ru_1Ir_1O_{16}$	1.37	1.35	1.75	0.45	0.52
$Sr_6Ir_2O_{16}$	0.62	1.17	1.56	1.57	0.34
RuO_2	0.26	1.10	1.76	1.79	0.56
IrO_2	0.30	1.38	1.84	1.40	0.61

3
4

1 **Supplementary Table 3 | The energy of ions in the solution used in the Pourbaix**
2 **diagram calculation.**

Reference	energy (eV)
Sr^{2+}(aq)	-5.844
RuO_4^{2-}(aq)	-3.105
RuO^+(aq)	-0.453
RuO(aq)	0.010
Ru^{2+}(aq)	1.557
Ru^{3+}(aq)	1.797
Ir^{3+}(aq)	0.347
IrO_4^{2-}(aq)	-2.038
H_2O(aq)	-2.458
H^+(aq)	0.000

3
4

Supplementary Table 4 | Summary of the stoichiometry of different catalysts.

Catalyst	Sr ratio[1]	Ru ratio	Ir ratio	Formula[2]
SrRuIr	0.22	0.65	0.13	$Sr_{1.7}Ru_5Ir_1O_{13.7}$
SrRu	0.24	0.76	-	$Sr_{1.6}Ru_5O_{11.6}$
RuIr	-	0.85	0.15	$Ru_5Ir_{0.9}O_{11.8}$

[1] Quantified according to STEM-EDX.

[2] Calculated by assuming the chemical valence of Sr, Ru, Ir and O are +2, +4, +4 and -2, respectively.

Supplementary Table 5 | Summary of electrochemical performance of different samples on GCE

Catalyst	Overpotential[1] (mV)	Tafel slope (mV dec^{-1})	TOF[2] (s^{-1})
SrRuIr	190±2	39	0.197±0.012
SrRu	238±1	51	0.063±0.004
RuIr	239±1	48	0.060±0.002
RuO$_2$	287±4	53	0.016±0.001
IrO$_2$	339±4	46	0.005±0.001

[1] Overpotential at 10 mA cm^{-2}.

[2] Calculated according to the mass loading of all atoms. η=300 mV.

1 **Supplementary Table 6 | BET surface area of different catalysts.**

Sample	BET surface area ($m^2\ g^{-1}$)	C	R
SrRuIr	14.41	78.9	0.9997
RuIr	6.06	174.8	0.9999
SrRu	5.37	1419.6	0.9990
RuO_2	7.62	201.6	0.9999
IrO_2	21.58	335.9	0.9997

2
3

Supplementary Table 7 | Performance summary of previous reported OER catalysts in acidic environment.

Catalyst	η^2	Mass activity	TOF/Methods	Stability	Reference
SrRuIr[1]	**180±5 mV** **210 mV (after 30h)** **216 mV (after 1000h)** **223 mV (after 1500h)**	**281 A $g_{nobel\ metal}^{-1}$ @ 270 mV** **429 A $g_{nobel\ metal}^{-1}$ @ 300 mV**	**0.13 s^{-1} @ 300 mV / nobel metal loading**	**1500h @ 10 mA cm^{-2}** **150h @ 1 A cm^{-2} in PEM**	**This work**
RuIr[1]	**218±2 mV** **250 mV (after 70h)**	**102 A $g_{nobel\ metal}^{-1}$ @ 270 mV** **200 A $g_{nobel\ metal}^{-1}$ @ 300 mV**	**0.059 s^{-1} @ 300 mV / nobel metal loading**	**70h @ 10 mA cm^{-2}**	**This work**
RuIrO$_x$ nano-netcage	233 mV ~17% j^3 decrease			24h @ 1.45V (full cell)	Ref.[16]
Mn-RuO$_2$	158 mV ~370 mV (after 10h)	596 A g_{Ru}^{-1} @ 270 mV	0.39 s^{-1} @250 mV / total Ru loading	10h @ 10 mA cm^{-2}	Ref.[17]
Cr$_{0.6}$Ru$_{0.4}$O$_2$ (550)	178 mV ~250 mV (after 10h)	229 A g_{cat}^{-1} @ 270 mV	0.15 s^{-1} @ 260 mV / total mass loading	10h @ 10 mA cm^{-2}	Ref.[18]
Ru@IrO$_x$	282 mV 10% j decrease	645 A g_{cat}^{-1} @ 330 mV		24h @ 1.55V vs. RHE	Ref.[19]
Co-RuIr	235 mV ~380 mV (after 25h)			25h @ 10 mA cm^{-2}	Ref.[20]
Ru$_1$–PtCu	220 mV ~250 mV (after 28h)	6615 A g_{Ru}^{-1} @ 280 mV 779 A g_{metal}^{-1} @ 280 mV		28h @ 10 mA cm^{-2}	Ref.[21]
Pd@Ru	257 mV 13% j decrease		0.10 s^{-1} @ 270 mV / total Ru loading	10h @ 1.45V vs. RHE	Ref.[22]
Cu-doped RuO$_2$	188 mV 271 mv (after 8h)		0.053 s^{-1} @ 250 mV / total Ru loading	8h @ 10 mA cm^{-2}	Ref.[23]
Y$_2$Ru$_2$O$_{7-\delta}$	190 mV (onset) ~290 mV[4]		0.055 s^{-1} @ 270 mV / Total Ru loading	8h @ 1 mA cm^{-2}	Ref.[24]

[1] Measured on carbon paper.

[2] Overpotential at 10 mA cm^{-2}.

[3] Current density.

[4] Overpotential at 1 mA cm^{-2} after 8h V-T test.

1   **Supplementary Table 8 | Stability number (S-number) of different catalysts.**

Catalysts	S-number after 6 h	S-number after 12 h
SrRuIr	10400	19717
SrRu	265	410

2
3

Supplementary Table 9 | Parameters used in EXAFS fittings.

Sample	Element	Path	CN	S_0^2	σ^2	E_0	R (Å)
SrRuIr	Ru K-edge	Ru-O 1#	6 (set)	0.78	0.0043±0.0003	3.16±1.22	1.990±0.005
		Ru-Ru 1#	1.45±0.44	0.78	0.0046±0.0013	-2.57±2.42	3.098±0.020
		Ru-Ir 1#	0.36	0.78	0.0046±0.0013	-2.57±2.42	3.086±0.103
		Ru-O 2#	4 (set)	0.78	0.0046±0.0013	-2.57±2.42	3.388±0.038
		Ru-Ru 2#	3.34±1.36	0.78	0.0046±0.0013	-2.57±2.42	3.546±0.023
		Ru-Ir 2#	0.83	0.78	0.0046±0.0013	-2.57±2.42	3.685±0.036
		Ru-Sr 1#	0.83	0.78	0.0046±0.0013	-2.57±2.42	3.635±0.155
	Ir L_3-edge	Ir-O 1#	6.01±0.25	0.85	0.0028±0.0004	4.91±0.82	1.971±0.005
		Ir-Ru 1#	2 (set)	0.85	0.0069±0.0007	1.57±2.08	3.100±0.021
		Ir-O 2#	4 (set)	0.85	0.0028±0.0004	4.91±0.82	3.568±0.045
		Ir-Ru 2#	7.19±1.51	0.85	0.0069±0.0007	1.57±2.08	3.556±0.018
RuO_2	Ru K-edge	Ru-O 1#	6 (set)	0.78	0.0018±0.0003	3.81±0.74	1.983±0.003
IrO_2	Ir L_3-edge	Ir-O 1#	6 (set)	0.85	0.0049±0.0005	3.72±3.52	2.002±0.025

Supplementary Table 10 | Mass spectroscopy peak area of different catalysts cycled in ^{18}O labeled electrolyte.

Sample	Scan No.	$^{34}O_2$ area (×10⁻¹⁰ a.u.)	$^{36}O_2$ area (×10⁻⁹ a.u.)	Area ratio ($^{34}O_2$: $^{36}O_2$)	LOM content (%)
SrRuIr	1	1.982	2.368	0.084	7.72
	2	1.659	1.951	0.085	7.83
	3	1.401	1.676	0.084	7.72
	4	1.312	1.494	0.088	8.07
	5	1.063	1.290	0.082	7.61
RuO$_2$	1	17.880	10.818	0.165	14.18
	2	9.823	5.917	0.166	14.24
	3	7.150	4.337	0.165	14.15
	4	6.469	3.780	0.171	14.61
	5	5.899	3.384	0.174	14.84

The mass spectroscopy signals are baseline subtracted.

Supplementary Table 11 | The deconvolution of O 1s XPS spectra using CasaXPS software.

Sample	Peak	Lineshape	Position (eV)	FWHM	Area
SrRuIr	lattice O	LA(1.53,243)	529.94	2.15	28842.15
	ads. OH	LA(1.53,243)	531.84	3.03	49249.27
	ads. H_2O	LA(1.53,243)	534.21	2.74	27015.19
RuO_2	lattice O	LA(1.53,243)	529.24	1.31	19026.94
	ads. OH	LA(1.53,243)	531.14	2.89	78033.58
	ads. H_2O	LA(1.53,243)	533.6	3.53	34039.74

The peak area ratio of adsorbted OH:lattcie O is 1.7 for SrRuIr and 4.1 for RuO_2, respectively.

1 **Supplementary Table 12 | The quantification parameters of Sr 3d, Ru 3p and Ir**
2 **4f XPS spectra using CasaXPS software.**

Sample	Peak	R.S.F.*	Raw Area	Atomic concentration	Sr:Ru:Ir
SrRuIr after 12 h	Sr 3d	5.29	2699.8	0.06	0.44:5:1.95
	Ir 4f	14.33	32319.5	0.27	
	Ru 3p*	2.84	16384.2	0.67	
SrRuIr after 24 h	Sr 3d	5.29	870.4	0.05	0.38:5:1.6
	Ir 4f	14.33	16539.4	0.23	
	Ru 3p	2.84	10247.2	0.72	

3 *R.S.F = Relative sensitivity factor
4 *The amount of Ru was quantified according to Ru $3p_{1/2}$ peak area.
5
6

1 **Supplementary Table 13 | Bader charge analysis in RuO$_2$ and SrRuIr surfaces.**

Model	Charge on active site Ru
RuO$_2$	+1.50
Sr$_1$Ru$_6$Ir$_1$O$_{16}$	+1.59
Sr$_2$Ru$_5$Ir$_1$O$_{16}$	+1.64
Sr$_2$Ru$_{5.5}$Ir$_{0.5}$O$_{16}$	+1.64
Sr$_2$Ru$_{1.5}$Ir$_{4.5}$O$_{16}$	+1.64
Sr$_2$Ru$_{3.5}$Ir$_{2.5}$O$_{16}$	+1.62
Sr$_2$Ru$_6$O$_{16}$	+1.64

2
3

1 **Supplementary Table 14 | Performance of PEM cells tested at 80°C, 1 A cm^{-2}.**

Catalysts	Cell voltage @ 1 A cm^{-2}	Stability test	Reference
SrRuIr	**1.50 V**	**150h @ 1 A cm^{-2}**	**This work**
$Ir_{0.7}Ru_{0.3}O_x$	1.59 V	1000h @ 1 A cm^{-2}	Ref.[25]
$Ru_{0.7}Ir_{0.3}O_2$	1.60 V		Ref.[26]
YBRO-0.15	1.64 V (60°C)	15h@ 150 mA cm^{-2}	Ref.[27]
$Ir_{0.7}Ru_{0.3}O_x$	1.70 V	400h @ 1 A cm^{-2}	Ref.[28]
$Ir_{0.6}Sn_{0.4}O_2$	1.70 V	100h @ 1 A cm^{-2}	Ref.[29]
IrO_2	1.65 V	1000h @ 1 A cm^{-2}	Ref.[30]
$Ir_{0.4}Ru_{0.6}Mo_xO_y$	1.61 V		Ref.[31]

2
3

1 **Supplementary Table 15 | Summary of parameters used in EIS fittings on GCE.**

Parameters	SrRuIr	SrRu	RuIr	RuO$_2$	IrO$_2$
R$_s$ (Ω)	8.45	9.05	8.52	9.92	8.31
R$_{ct}$ (Ω)	508.2	600.4	581.4	1447.5	12557
CPE.Y$_0$ (mF s$^{\alpha-1}$)	1.26	0.23	0.87	0.56	0.19
CPE.α	0.85	0.92	0.95	0.94	0.93
C$_{dl}$ (mF)	642.0	145.0	691.3	398.6	116.8
ECSA (cm^2)	18.34	4.14	19.75	11.39	3.34

2
3

References

(1) Zhang, B.; Zheng, X.; Voznyy, O.; Comin, R.; Bajdich, M.; Garcia-Melchor, M.; Han, L.; Xu, J.; Liu, M.; Zheng, L.; Garcia de Arquer, F. P.; Dinh, C. T.; Fan, F.; Yuan, M.; Yassitepe, E.; Chen, N.; Regier, T.; Liu, P.; Li, Y.; De Luna, P.; Janmohamed, A.; Xin, H. L.; Yang, H.; Vojvodic, A.; Sargent, E. H., Homogeneously dispersed multimetal oxygen-evolving catalysts. *Science* **2016,** *352* (6283), 333-337.

(2) McCrory, C. C.; Jung, S.; Peters, J. C.; Jaramillo, T. F., Benchmarking heterogeneous electrocatalysts for the oxygen evolution reaction. *J. Am. Chem. Soc.* **2013,** *135* (45), 16977-16987.

(3) Geiger, S.; Kasian, O.; Ledendecker, M.; Pizzutilo, E.; Mingers, A. M.; Fu, W. T.; Diaz-Morales, O.; Li, Z.; Oellers, T.; Fruchter, L.; Ludwig, A.; Mayrhofer, K. J. J.; Koper, M. T. M.; Cherevko, S., The stability number as a metric for electrocatalyst stability benchmarking. *Nat. Catal.* **2018,** *1* (7), 508-515.

(4) Ravel, B.; Newville, M., ATHENA, ARTEMIS, HEPHAESTUS: data analysis for X-ray absorption spectroscopy using IFEFFIT. *J. Synchrotron Rad.* **2005,** *12*, 537-541.

(5) Xia, Z.; Zhang, H.; Shen, K.; Qu, Y.; Jiang, Z., Wavelet analysis of extended X-ray absorption fine structure data: Theory, application. *Physica B: Condensed Matter* **2018,** *542*, 12-19.

(6) Funke, H.; Scheinost, A. C.; Chukalina, M., Wavelet analysis of extended X-ray absorption fine structure data. *Phys. Rev. B* **2005,** *71* (9), 094110.

(7) Xia, Z. A tool to make wavelet transformation of EXAFS. https://github.com/hellozhaoming/wtexfas.

(8) Funke, H.; Chukalina, M.; Scheinost, A. C., A new FEFF-based wavelet for EXAFS data analysis. *J. Synchrotron Rad.* **2007,** *14* (Pt 5), 426-432.

(9) Boman, C.-E.; Danielsen, J.; Haaland, A.; Jerslev, B.; Schäffer, C. E.; Sunde, E.; Sørensen, N. A., Refinement of the crystal structure of ruthenium dioxide. *Acta Chem. Scand.* **1970,** *24*, 116-122.

(10) Seitz, L. C.; Dickens, C. F.; Nishio, K.; Hikita, Y.; Montoya, J.; Doyle, A.; Kirk, C.; Vojvodic, A.; Hwang, H. Y.; Norskov, J. K.; Jaramillo, T. F., A highly active and stable $IrO_x/SrIrO_3$ catalyst for the oxygen evolution reaction. *Science* **2016,** *353* (6303), 1011-1014.

(11) Chang, S. H.; Danilovic, N.; Chang, K. C.; Subbaraman, R.; Paulikas, A. P.; Fong, D. D.; Highland, M. J.; Baldo, P. M.; Stamenkovic, V. R.; Freeland, J. W.; Eastman, J. A.; Markovic, N. M., Functional links between stability and reactivity of strontium ruthenate single crystals during oxygen evolution. *Nat. Commun.* **2014,** *5*, 4191.

(12) Chen, Y.; Li, H.; Wang, J.; Du, Y.; Xi, S.; Sun, Y.; Sherburne, M.; Ager, J. W., 3rd; Fisher, A. C.; Xu, Z. J., Exceptionally active iridium evolved from a pseudo-cubic perovskite for oxygen evolution in acid. *Nat. Commun.* **2019,** *10* (1), 572.

(13) Gauthier, J. A.; Dickens, C. F.; Chen, L. D.; Doyle, A. D.; Nørskov, J. K., Solvation effects for oxygen evolution reaction catalysis on IrO_2(110). *J. Phys. Chem. C* **2017,** *121* (21), 11455-11463.

(14) Zhang, Y.; Huang, L.; Arunagiri, T. N.; Ojeda, O.; Flores, S.; Chyan, O.; Wallace, R. M., Underpotential deposition of copper on electrochemically prepared conductive ruthenium oxide surface. *Electrochem. Solid-State Lett.* **2004,** *7* (9).

(15) Zagalskaya, A.; Alexandrov, V., Role of defects in the interplay between adsorbate evolving and lattice oxygen mechanisms of the oxygen evolution reaction in RuO_2 and IrO_2. *ACS Catal.* **2020,** *10* (6), 3650-3657.

(16) Zhuang, Z.; Wang, Y.; Xu, C. Q.; Liu, S.; Chen, C.; Peng, Q.; Zhuang, Z.; Xiao, H.; Pan, Y.; Lu, S.; Yu, R.; Cheong, W. C.; Cao, X.; Wu, K.; Sun, K.; Wang, Y.; Wang, D.; Li, J.; Li, Y., Three-dimensional open nano-netcage electrocatalysts for efficient pH-universal overall water splitting. *Nat. Commun.* **2019,** *10* (1), 4875.

(17) Chen, S.; Huang, H.; Jiang, P.; Yang, K.; Diao, J.; Gong, S.; Liu, S.; Huang, M.; Wang, H.; Chen, Q., Mn-doped RuO_2 nanocrystals as highly active electrocatalysts for enhanced oxygen evolution in acidic media. *ACS Catal.* **2019,** *10* (2), 1152-1160.

(18) Lin, Y.; Tian, Z.; Zhang, L.; Ma, J.; Jiang, Z.; Deibert, B. J.; Ge, R.; Chen, L., Chromium-ruthenium oxide solid solution electrocatalyst for highly efficient oxygen evolution reaction in acidic media. *Nat. Commun.* **2019,** *10* (1), 162.

(19) Shan, J.; Guo, C.; Zhu, Y.; Chen, S.; Song, L.; Jaroniec, M.; Zheng, Y.; Qiao, S.-Z., Charge-redistribution-enhanced nanocrystalline $Ru@IrO_x$ electrocatalysts for oxygen evolution in acidic media. *Chem* **2019,** *5* (2), 445-459.

(20) Shan, J.; Ling, T.; Davey, K.; Zheng, Y.; Qiao, S. Z., Transition-metal-doped RuIr bifunctional nanocrystals for overall water splitting in acidic environments. *Adv. Mater.* **2019,** *31* (17), e1900510.

(21) Yao, Y.; Hu, S.; Chen, W.; Huang, Z.-Q.; Wei, W.; Yao, T.; Liu, R.; Zang, K.; Wang, X.; Wu, G.; Yuan, W.; Yuan, T.; Zhu, B.; Liu, W.; Li, Z.; He, D.; Xue, Z.; Wang, Y.; Zheng, X.; Dong, J.; Chang, C.-R.; Chen, Y.; Hong, X.; Luo, J.; Wei, S.; Li, W.-X.; Strasser, P.; Wu, Y.; Li, Y., Engineering the electronic structure of single atom Ru sites via compressive strain boosts acidic water oxidation electrocatalysis. *Nat. Catal.* **2019,** *2* (4), 304-313.

(22) Hu, Y.; Luo, X.; Wu, G.; Chao, T.; Li, Z.; Qu, Y.; Li, H.; Wu, Y.; Jiang, B.; Hong, X., Engineering the atomic layer of RuO_2 on PdO nanosheets boosts oxygen evolution catalysis. *ACS Appl. Mater. Interfaces* **2019,** *11* (45), 42298-42304.

(23) Su, J.; Ge, R.; Jiang, K.; Dong, Y.; Hao, F.; Tian, Z.; Chen, G.; Chen, L., Assembling ultrasmall copper-doped ruthenium oxide nanocrystals into hollow porous polyhedra: Highly robust electrocatalysts for oxygen evolution in acidic media. *Adv. Mater.* **2018**, e1801351.

(24) Kim, J.; Shih, P. C.; Tsao, K. C.; Pan, Y. T.; Yin, X.; Sun, C. J.; Yang, H., High-performance pyrochlore-type yttrium ruthenate electrocatalyst for oxygen evolution reaction in acidic media. *J. Am. Chem. Soc.* **2017,** *139* (34), 12076-12083.

(25) Siracusano, S.; Baglio, V.; Van Dijk, N.; Merlo, L.; Aricò, A. S., Enhanced performance and durability of low catalyst loading PEM water electrolyser based on a short-side chain perfluorosulfonic ionomer. *Appl. Energy* **2017,** *192*, 477-489.

(26) Xu, W.; Scott, K., The effects of ionomer content on PEM water electrolyser membrane electrode assembly performance. *Int. J. Hydrogen Energy* **2010,** *35* (21), 12029-12037.

(27) Feng, Q.; Zou, J.; Wang, Y.; Zhao, Z.; Williams, M. C.; Li, H.; Wang, H., Influence of surface oxygen vacancies and ruthenium valence state on the catalysis of pyrochlore oxides. *ACS Appl. Mater. Interfaces* **2020,** *12* (4), 4520-4530.

(28) Wang, L.; Saveleva, V. A.; Zafeiratos, S.; Savinova, E. R.; Lettenmeier, P.; Gazdzicki, P.; Gago, A. S.; Friedrich, K. A., Highly active anode electrocatalysts derived from electrochemical leaching of Ru from metallic $Ir_{0.7}Ru_{0.3}$ for proton exchange membrane electrolyzers. *Nano Energy* **2017,** *34*, 385-391.

(29) Jiang, G.; Yu, H.; Hao, J.; Chi, J.; Fan, Z.; Yao, D.; Qin, B.; Shao, Z., An effective oxygen electrode based on $Ir_{0.6}Sn_{0.4}O_2$ for PEM water electrolyzers. *J. Energy Chem.* **2019,** *39*, 23-28.

(30) Siracusano, S.; Baglio, V.; Grigoriev, S. A.; Merlo, L.; Fateev, V. N.; Aricò, A. S., The influence of iridium chemical oxidation state on the performance and durability of oxygen evolution catalysts in PEM electrolysis. *J. Power Sources* **2017,** *366*, 105-114.

(31) Cheng, J.; Zhang, H.; Ma, H.; Zhong, H.; Zou, Y., Preparation of $Ir_{0.4}Ru_{0.6}Mo_xO_y$ for oxygen evolution by modified Adams' fusion method. *Int. J. Hydrogen Energy* **2009,** *34* (16), 6609-6613.